

**UCSF**

**UC San Francisco Electronic Theses and Dissertations**

**Title**

Hardware and software developments for high field ( $\geq 3$ T) MRI

**Permalink**

<https://escholarship.org/uc/item/26k9b6c4>

**Author**

von Morze, Cornelius Jan

**Publication Date**

2008-01-22

Peer reviewed|Thesis/dissertation

Hardware and software developments for high field ( $\geq 3\text{T}$ ) phased array MRI  
by

Cornelius Jan von Morze

DISSERTATION

Submitted in partial satisfaction of the requirements for the degree of

DOCTOR OF PHILOSOPHY

in

Bioengineering

in the

GRADUATE DIVISION

of the

UNIVERSITY OF CALIFORNIA, SAN FRANCISCO

AND

UNIVERSITY OF CALIFORNIA, BERKELEY



### *Acknowledgements*

I owe the greatest debt for the success in my graduate work to my graduate advisor, Dan Vigneron, and also to my co-workers in the UCSF Radiology labs, especially Duan Xu, Suchandrima Banerjee, Kostas Karpodinis, Lucas Carvajal, Janine Lupo, Srivathsa Veeraraghavan, Meredith Metcalf, and Albert Chen, to the brilliant industrial scientists Jim Tropp and Doug Kelley, to my dissertation committee members Sharmila Majumdar and Jim Barkovich, to the extraordinary clinicians / researchers Derk Purcell, Chris Hess, and Pratik Mukherjee, and to all the professors and GSI's involved in my graduate curriculum. But most of all, I want to thank my wonderful parents and big brother Len, whose unconditional love and support have helped me the most. Thanks to you all !



## Hardware and software developments for high field ( $\geq 3T$ ) phased array MRI

Cornelius Jan von Morze

Key engineering challenges associated with realizing the full potential of high field MRI are the design of phased array RF coils, the development of parallel imaging techniques for rapid imaging, and the determination of optimal acquisition parameters for various clinical applications. Parallel imaging techniques, which are enabled by phased array RF coils, take advantage of higher MRI field strengths by trading the higher SNR for imaging speed. I constructed a novel eight-channel non-overlapping phased array RF coil with capacitive decoupling for imaging of the brain and the hip, which was designed to minimize reconstruction-related SNR losses in parallel imaging. The design was aided by high frequency electromagnetic simulations that I programmed, and the coil was tested in various clinical applications, demonstrating quantitative performance improvements over a commercial eight-channel head coil. Higher field strengths improve the capability of intracranial time-of-flight MR angiography, an important fully non-invasive angiographic technique, due to the higher baseline SNR and the improved background suppression that is a result of longer T1 relaxation times. I optimized the acquisition protocol for 7T intracranial MRA, relying on a combination of simulations and experiments, and quantitatively verified the performance improvements over 3T. Using GRAPPA-based parallel imaging acquisition and reconstruction techniques that I developed, I designed a very high resolution ( $0.146\text{mm}^3$ ) protocol for 7T imaging of volunteers and patients with vascular disease. These techniques produced angiograms free from artifacts in all subjects, and correctly identified vascular pathology in patients.

# Table of contents

1	Introduction.....	1
2	Background.....	4
2.1	Fundamentals of magnetic resonance imaging.....	4
2.1.1	Overview.....	4
2.1.2	Precession and resonance.....	4
2.1.3	Bloch equations.....	7
2.1.4	Signal detection.....	8
2.1.5	Localization.....	9
2.1.6	Signal-to-noise ratio (SNR).....	11
2.1.7	Practical aspects of MRI pulse sequences.....	12
2.2	Phased array RF receiver coils.....	14
2.2.1	Volume coils vs. surface coils.....	14
2.2.2	Phased array image combination.....	16
2.3	Parallel imaging techniques.....	17
2.3.1	Overview.....	17
2.3.2	SENSE.....	18
2.3.3	SMASH.....	24
2.4	Imaging of neurovascular disease.....	25
2.4.1	Overview of neurovascular diseases.....	25
2.4.2	Catheter angiography.....	26
2.4.3	US / CTA / MRA.....	27
3	Development of novel non-overlapping, capacitively decoupled phased array coils for conventional and parallel imaging.....	30
3.1	Overview.....	30
3.2	Motivation for non-overlapping design.....	30
3.3	Non-overlapping coil design.....	32
3.3.1	SENSE simulations for optimizing coil geometry.....	32
3.3.2	Construction.....	34
3.3.3	Tuning and matching.....	35
3.3.4	Decoupling.....	37
3.3.5	Preamplifier and transmission line (T-line) considerations.....	41
3.4	Results.....	42
3.4.1	SENSE simulations.....	42
3.4.2	Decoupling.....	44
3.5	Discussion.....	45
3.6	Conclusions.....	46
3.7	Non-overlapping phased array coil for a MRI-compatible neonatal incubator.....	47
3.7.1	Background.....	47
3.7.2	Purpose.....	47
3.7.3	Design constraints.....	48
3.7.4	Design optimization.....	48
4	Clinical applications of the novel eight-channel nonoverlapping receive coil.....	52
4.1	Overview.....	52

4.2	Parallel diffusion weighted imaging (DWI) of the brain .....	52
4.2.1	DWI background.....	52
4.2.2	Parallel DWI human studies using ssEPI-SENSE .....	54
4.3	Magnetic resonance spectroscopic imaging (MRSI) of the brain .....	57
4.3.1	MRSI background.....	57
4.3.2	MRSI human studies .....	57
4.4	High resolution autocalibrating parallel MRI of trabecular bone in the hip .....	59
4.4.1	High resolution MRI of trabecular bone .....	59
4.4.2	b-SSFP with parallel imaging .....	59
4.4.3	Human hip studies.....	60
5	Intracranial Time-of-Flight (TOF) MRA at 7T using Phased Array Coils.....	63
5.1	TOF Technique.....	63
5.1.1	TOF Background.....	63
5.1.2	TOF Contrast .....	64
5.1.3	TOF artifacts and flow compensation .....	64
5.1.4	Simulations for TOF contrast optimization.....	65
5.1.5	Multiple overlapping thin slab acquisition (MOTSA) technique .....	67
5.1.6	Clinical applications of TOF MRA.....	68
5.2	TOF MRA human studies at 7T with comparison to 3T .....	68
5.2.1	Overview .....	68
5.2.2	Methods .....	70
5.2.3	Results .....	72
5.2.4	Discussion.....	77
5.2.5	Conclusion .....	80
6	Accelerated autocalibrating high resolution TOF MRA at 7T.....	82
6.1	Overview .....	82
6.2	Generalized autocalibrating partially parallel acquisition (GRAPPA) imaging ..	83
6.2.1	GRAPPA overview .....	83
6.2.2	GRAPPA reconstruction .....	83
6.3	Methods.....	85
6.4	Results.....	87
6.5	Discussion .....	92
7	Summary .....	94
8	References.....	96

## List of figures

Figure 2.1	SENSE simulations	23
Figure 3.1	Transverse magnetic field contour map for six-element array	34
Figure 3.2	Dual paddles comprising the eight-channel non-overlapping phased array coil	36
Figure 3.3	Experimental / simulated images from three-channel array with small amount of residual coupling	39
Figure 3.4	Mesh impedance matrix for three-channel non-overlapping phased array, circuit diagram	40
Figure 3.5	Smith chart polar plot of preamplifier reflection coefficient S11 in complex plane	43
Figure 3.6	Coil schematics and g-factor maps for comparable overlapping and non-overlapping designs	44
Figure 3.7	Schematic of non-overlapping array, showing final capacitor values implemented in the array, and coil dimensions	45
Figure 3.8	Individual coil images from an FSE scan	46
Figure 3.9	MRI compatible neonatal incubator and end-view of insert birdcage RF coil	49
Figure 3.10	G-factor map for proposed neonatal coil with R=2 along x, with proposed coil geometry	51
Figure 4.1	ssEPI diffusivity maps acquired with and without SENSE (R=2)	55
Figure 4.2	Axial and coronal color-coded anisotropy maps, demonstrating capability of EPI-SENSE HARDI acquisition to identify detailed fiber tract anatomy	57
Figure 4.3	Spectra with SNR of 20.7 for NAA peak	59
Figure 4.4	Fully-encoded coronal FIESTA image of hip alongside rate-4 GRAPPA accelerated acquisition for same slice	62
Figure 5.1	Surface contrast plot showing dependence of vessel contrast on TR and flip angle, for a given blood inflow velocity of 0.5 m/s	68
Figure 5.2	Comparison of 3T and 7T images in a normal volunteer	74
Figure 5.3	Mean CNR for 3T and 7T acquisitions grouped by arterial segment	75
Figure 5.4	Average CNR values obtained using improved acquisition parameters	76
Figure 5.5	Axial MIP's from two normal adult volunteers at both field strengths	77
Figure 5.6	Sagittal MIP through right half of 7T MRA data with removal of superficial calvarium and scalp soft tissues	78
Figure 6.1	Axial MIP's (8mm) through the same imaging region using standard GRAPPA, with increased artifact, and the customized autocalibrating reconstruction	89
Figure 6.2	Full axial MIP's through MRA images from same volunteer using original lower resolution protocol and higher resolution protocol with parallel imaging	90

## List of tables

Table 3.1	Ranges of coil design simulation parameters	50
-----------	---	----

# 1 Introduction

Over the past few decades, magnetic resonance imaging (MRI) has revolutionized diagnostic medicine by providing highly localized, three-dimensional images of the human body in a fully non-invasive manner. MRI acquisitions can be tailored to yield many useful sets of images that reflect a wide variety of contrast mechanisms. For each of these scans, the quality of the images and thus the diagnostic information obtainable from them is highly dependent on various hardware and software factors. These complicated dependencies make the fields of MR hardware and software engineering rich areas of research.

Arguably, the most important hardware factors that influence scanner capabilities are the main magnetic field strength and the design of the radiofrequency (RF) receiver coils. Higher magnetic field strengths and RF coils with increasing numbers of receivers can increase the system capabilities, if the associated engineering challenges are overcome. Examples of some key software factors are pulse timing and amplitude, total acquisition time, and choice of reconstruction technique. Much of the work in this dissertation was devoted to studying the effects of such hardware and software MRI parameters, developing improved methods or re-engineering them entirely where required.

Multi-channel RF receiver coils in particular offer great advantages for many MRI applications. They offer improved sensitivity in conventional imaging, and they enable accelerated imaging through recently developed parallel imaging techniques. Accelerated

imaging results in higher resolution or greater imaging coverage for a fixed acquisition time, or a faster scan with given resolution and coverage, resulting in various application-specific advantages. However, multi-channel coils introduce several engineering design challenges, including optimizing coil positioning, eliminating crosstalk between receivers, and optimally reconstructing larger amounts of data.

As a key part of this dissertation work, I designed and developed a novel eight-channel non-overlapping RF phased array coil for 3T imaging of the head and hip. The specific non-overlapping coil geometry was carefully selected on the basis of improved SNR and parallel imaging performance predicted from electromagnetic simulation software that I developed. To deal with the associated challenge of increased crosstalk between nearest neighbor elements in the array, I utilized advanced high frequency electrical engineering concepts to develop a novel intercoil capacitive decoupling network, and to manage interactions between low impedance preamplifiers and transmission line cabling for maximum decoupling. I tested the coil in various clinical applications in the head and hip, and demonstrated performance improvements.

Given the tremendous incidence of vascular disease in modern society, an extremely important clinical application of phased array MRI is magnetic resonance angiography (MRA), a non-invasive alternative to conventional catheter angiography. As will be described in later chapters, the capabilities of MRA theoretically could be greatly improved at higher field strengths and with larger numbers of RF receivers.

In another key part of this thesis, I developed an optimized protocol for 7T intracranial time-of-flight (TOF) MRA, a fully non-invasive angiographic technique with excellent spatial resolution and coverage. I optimized the key acquisition parameters through a combination of computer simulations that I developed and testing of different values of these parameters in human experiments. To enable scans at the highest possible resolution within a clinically feasible scan time, I also developed the software tools needed for parallel imaging acquisition and reconstruction of large amounts of data (i.e. ~ 4.5 Gigabytes of raw image data per high resolution angiographic study). I verified the performance improvements achievable using this technique over state-of-the-art 3T studies, and applied the technique to clinical studies of patients with cerebrovascular diseases.



## 2 Background

### 2.1 *Fundamentals of magnetic resonance imaging*

#### 2.1.1 Overview

MRI is ultimately based on nuclear magnetic resonance (NMR), which was discovered by Bloch and Purcell in 1946 [1, 2]. As a result of their angular momentum, atomic nuclei with an odd number of protons or neutrons have a small non-zero magnetic vector field associated with them, also described by an associated single vector magnetic dipole moment or “spin”. The basis of NMR/ MRI is the manipulation and detection of spins. Of the nuclear species that have this characteristic (such as  $^1\text{H}$ ,  $^{13}\text{C}$ ,  $^{19}\text{F}$ ,  $^{23}\text{N}$ ,  $^{31}\text{P}$ ), the nucleus of  $^1\text{H}$  (a single proton) is the most important to MRI due to its naturally high concentration in the human body as part of the water molecule.

#### 2.1.2 Precession and resonance

When placed in the main magnetic field of an MRI scanner, spins precess about the direction of the field. The exact origin of nuclear magnetism is quantum mechanical in nature and beyond the scope of this bioengineering dissertation, but for most purposes a spin may be viewed as equivalent to a tiny classical electric current loop, which also has an associated magnetic field and moment  $\mu$  [3]. From classical magnetostatics, a current loop placed in a constant external magnetic field  $B$  experiences no net force but a net torque

$$\vec{\tau} = \vec{\mu} \times \vec{B} \quad (2.1)$$

This torque effects a change in angular momentum  $J$  of the spin

$$\frac{d\vec{J}}{dt} = \vec{\tau} \quad (2.2)$$

Combining these two equations with the empirical result that the magnetic moment of a spin  $u$  is directly proportional to its angular momentum  $J$  by the gyromagnetic ratio ( $\gamma$ , specific to the nuclear species), we obtain the fundamental equation of motion for spins placed in an external magnetic field:

$$\frac{d\vec{\mu}}{dt} = \gamma\vec{\mu} \times \vec{B} \quad (2.3)$$

The solution for this vector differential equation describes the response of the spins to the applied field. For a main field along  $z$ , the solution in Cartesian coordinates is

$$\begin{aligned} \mu_x(t) &= \mu_x(0) \cos(\omega t) + \mu_y(0) \sin(\omega t) \\ \mu_y(t) &= \mu_y(0) \cos(\omega t) - \mu_x(0) \sin(\omega t) \\ \mu_z(t) &= \mu_z(0) \end{aligned} \quad (2.4)$$

These equations describe precession about  $z$  at an angular velocity given by the Larmor frequency

$$\omega = \gamma |\vec{B}| \quad (2.5)$$

The main field strength of most MRI scanners is 1.5T, and the gyromagnetic ratio for  $^1\text{H}$  is 42.6MHz/T, so the Larmor frequency for protons is about 64 MHz (in the radiofrequency or RF range of the electromagnetic spectrum). For the 3T and 7T high field systems studied in this dissertation, the Larmor frequencies are about 128MHz and 300MHz.  $B$  and thus  $\omega$  varies slightly *in vivo* due to differences in magnetic susceptibility among different tissues and air, which can result in imaging artifacts.

In reality, the initial condition on  $u$  for a spin is restricted to only two possible values from quantum mechanics [3], namely

$$\bar{\mu} = \pm \frac{\gamma h \sqrt{3}}{4\pi} \angle 54.7^\circ \text{ off z-axis} \quad (2.6)$$

So, a spin actually precesses along a cone with a central axis set by the main field direction.

In any substantial collection of spins precessing around the main field, there is no phase coherence and thus no net bulk magnetization to measure [4]. Spin signal detection is achieved by rotating spins coherently into the plane transverse to the main field. This is accomplished using RF magnetic pulses applied transverse to the main field direction. Viewing a precessing spin in a rotating reference frame that is co-rotating about the main field direction at the same frequency as the spin is precessing (the Larmor frequency), spins are stationary. Since it has already been established that spins precess about an applied magnetic field, in a manner exactly the same as described above (if the relaxation effects that have yet to be described are ignored), an additional static magnetic field  $B_1$  (which is actually rotating at the Larmor frequency in the laboratory frame) transverse to the main field direction produces an additional rotation of the spin about this transverse axis, while the spin also continues to rotate about the main field in the laboratory frame. Practically, this rotation is achieved through the application of a circularly polarized RF pulse in the transverse plane (typically ms in duration, and a small fraction of a Gauss in amplitude). The equation for the rotation angle, or “flip angle”, is given by

$$\theta = \gamma |B_1| t \quad (2.7)$$

where  $t$  is the pulse duration. This is a resonant phenomenon since only an RF pulse at the Larmor frequency will tip spins into the transverse plane.

### 2.1.3 Bloch equations

Corrections to equation (2.3) are necessary when considering spins within materials due to interactions of the spins with their surroundings, known as T1 and T2 relaxation processes [5]. This is encapsulated by adding two terms to the fundamental equation of motion given above, forming the Bloch equation for bulk magnetization  $\vec{M}$

$$\frac{d\vec{M}}{dt} = \vec{M} \times \gamma\vec{B} - \frac{M_x\hat{x} + M_y\hat{y}}{T_2} - \frac{(M_z - M_{z,0})\hat{z}}{T_1} \quad (2.8)$$

In addition to describing precession (first term), this equation also captures the exponential decay and recovery of components of the magnetization (second and third terms).

Taking a typical initial condition corresponding to magnetization purely in the transverse plane along x (i.e. following a 90-degree pulse), the solutions to (2.8) are

$$\begin{aligned} M_x(t) &= M_0 e^{-\frac{t}{T_2}} \cos(\omega t) \\ M_y(t) &= M_0 e^{-\frac{t}{T_2}} \sin(\omega t) \\ M_z(t) &= M_0 \left( 1 - e^{-\frac{t}{T_1}} \right) \end{aligned} \quad (2.9)$$

So after being rotated into the transverse plane by an RF pulse, they continue to precess about z at the Larmor frequency, decay in their transverse components according to T2, and refresh in the longitudinal direction according to T1. Typical water proton T2 values are on the order of 100 ms, while T1 values are on the order of seconds. The T1 and T2 relaxation times are characteristic of water within certain tissue types. For example, the relaxation times for water in fat are much less than that for water in muscle. Differences

in T1 and T2 relaxation times are the most important source of contrast in MR images, yielding soft tissue contrast, and the differences are highlighted by appropriately setting the timing parameters in MRI pulse sequences according to the T1 and T2 times of the tissues concerned.

#### 2.1.4 Signal detection

Coherent precession of spins in the transverse plane produces a non-zero time-varying magnetic field throughout space, which can be detected in a pickup coil through Faraday's law of induction [6]. The time-varying magnetic flux, or net magnetic field summed over the detector coil surface, produces a voltage in the coil. This is described by

$$V = -\frac{d}{dt} \oiint_{coil} \bar{B}_{spins} \cdot d\bar{s} \quad (2.10)$$

For spins precessing at one frequency, this can be re-written in complex form as

$$V = -j\omega \oiint_{coil} \bar{B}_{spins,complex} \cdot d\bar{s}, \text{ where } \text{Re}\{\bar{B}_{spins,complex} e^{j\omega t}\} = \bar{B}_{spins} \quad (2.11)$$

(side note: this relationship between complex field quantities and the actual fields will always be assumed.) However, it is more useful to think of the MRI signal as a summation of spin signals over space. Under certain conditions, it is possible to rewrite the coil signal as a spatial integral of the spin magnetization multiplied by the complex magnetic field produced by a unit current in the coil [7]

$$V = \frac{j\omega}{I_c} \int_{sample} \bar{B}_c \cdot \bar{M} dV \quad (2.12)$$

Thus the receive pattern for a coil is essentially equal to the complex magnetic field produced by unit current in the coil. This illustrates the principle of reciprocity in MRI.

However, this equation is based on the assumption of low field strength (low frequency). At higher field strengths (such as 3T and 7T), the transmit and receive patterns for a coil are increasingly different due to the gyrotropism of spins [7].

### 2.1.5 Localization

Small spatially linear gradient fields are added to the main magnetic field in order to localize spins in MRI [8]. Taking advantage of the linear dependence of the precessional frequency on the total main field, these additional fields produce spatially dependent frequency shifts in the spins, which allow signals to be localized by controlled changes to their frequencies and phases.

The typical first step in localization is the application of a spatially selective RF excitation pulse (known as slice selection) [5]. A linear gradient along the main axis (i.e. z) is applied while a perpendicular, frequency selective RF pulse (bandpass) is applied that resonates with and rotates into the transverse plane only the spins within a certain frequency range or slice of space perpendicular to the axis. In a 2D sequence, this slice is thin, and only localization in the transverse directions (x,y) is still required.

Following the slice selective excitation pulse, the signal equation for the excited slice as a function of time, under the influence of linear x and y gradients (following demodulation to base-band to reflect only gradient-induced precession, and ignoring relaxation), is [5]

$$S(t) = \int_x \int_y M(x,y) e^{-2\pi j [k_x(t)x + k_y(t)y]} dx dy, \text{ where} \quad (2.13)$$

$$\begin{aligned}
k_x(t) &= \frac{\gamma}{2\pi} \int_0^t G_x(\tau) d\tau \\
k_y(t) &= \frac{\gamma}{2\pi} \int_0^t G_y(\tau) d\tau
\end{aligned} \tag{2.14}$$

This is based on (2.12) with the assumption of uniform transmission and reception coil profiles, and ignoring constant factors. Data is recorded over time as a function of known applied gradient histories to enable inversion of this equation. Comparing this equation to the 2D Fourier transform (2DFT) of the magnetization  $M(x,y)$ ,

$$M_{2DFT}(k_x, k_y) = \int_x \int_y M(x, y) e^{-2\pi j(k_x x + k_y y)} dx dy \tag{2.15}$$

it is apparent that

$$S(t) = M_{2DFT}(k_x(t), k_y(t)) \tag{2.16}$$

So by applying main field gradients along  $x$  and  $y$ , the 2DFT of the magnetization can be measured over time, and a 2D map of the magnetization can be obtained by an inverse 2DFT on the data. In 3D methods, the selected slice is large (like a slab), and the 3DFT of the magnetization is sampled. The 2D or 3D spatial frequency domain over which MRI data is acquired is known as “k-space”. Time is mapped to the k-space position based on knowledge of  $G(t)$ , and  $S(t)$  becomes  $S(k)$ .

The extremely important effects of discrete and finite sampling of MRI data, which determine the imaging field of view and spatial resolution, respectively, [4] are described in Sec 2.3 on parallel imaging techniques.

### 2.1.6 Signal-to-noise ratio (SNR)

At the magnetic field strengths used in the research described in this dissertation, noise due to thermal motion of electrons in the sample (known as Johnson noise) is the primary source of noise in MR images [9]. Signal-to-noise ratio (SNR) is a key limiting factor in MR imaging, and is defined as signal divided by the standard deviation of the noise (since the noise is expected to be zero mean). SNR in MRI obeys the approximate scaling relationship (that can be expressed in various forms)

$$SNR \propto \frac{\omega * B1 * M dV}{\omega r_c^2} \propto \frac{B_0}{r_c^3} dV \propto B_0 \frac{dV}{V} = \frac{B_0}{N^3} \quad (2.17)$$

where  $B_0$  is the main field strength,  $M$  is the voxel magnetization,  $r_c$  is the receiver coil radius (assuming a cylindrical coil),  $B_1$  is the magnetic field per unit current for the receiver coil (depends on  $r_c$ ),  $V$  is the sample volume, and  $N$  is the matrix size [9]. According to these relationships, the main factors that influence SNR are main field strength, receiver coil size, and the voxel magnetization (or equivalently, the spatial resolution of the acquisition).

The above expression ignores a few other key effects on SNR. First, the above expression is for a uniform receiver coil. Noise is spread uniformly across any single coil image due to a property of the FT [4], but when using surface coils, the signal and thus SNR varies with position in the sample. SNR may vary in much more complicated ways depending on the choice of reconstruction technique. Second, this expression also ignores sequence parameters like flip angle and  $T_1$  and  $T_2$  relaxation times, which can have a huge effect on SNR. Lastly, it ignores the effect of imaging time. With a greater number of phase



encoding steps, SNR is built up according to the square root of the imaging time through signal averaging (through the convergence of noise to zero mean) [5].

All of these influences on SNR must be considered in order to engineer a successful MRI scan.

### **2.1.7 Practical aspects of MRI pulse sequences**

#### *Frequency and phase encoding*

Practically, one line of k-space is usually read out at a time, by activating a gradient while collecting data, a process called “frequency encoding”. This process is repeated for several sequential “phase encoding” steps. For each phase encoding step, a different gradient lobe area is applied to spins following RF excitation and just before frequency encoding. Together, these methods introduce the correct frequency and phase shifts on the spins to set up sampling of their 2D or 3DFT.

#### *Repetition time and T1 contrast*

The interval between each phase encoding step is known as the repetition time, or TR. Since the exponential recovery of longitudinal magnetization of different spins occurs at different rates following each RF excitation according to their T1 relaxation times, the TR is often a key timing parameter for resultant T1 contrast in the images. Up to the point of signal loss due to saturation, a shorter TR results in more T1 contrast, or T1-weighting.

#### *Echo time and T2 contrast*

From (2.15), maximum signal is obtained when the center of k-space is traversed (i.e. when the net gradient history is zero, and all spins are in phase), and much less is measured at the edges due to gradient-induced dephasing. The point of maximum signal is called the echo, and the time between the RF excitation and the echo is known as the echo time, or TE. Passing through the echo is known as refocusing. While gradient-induced phase is reversible and can be refocused at will, spins also dephase due to T2 relaxation, which is irreversible, as well as due to small inhomogeneities in the main magnetic field (T2'), which are not reversible by gradients. Together these effects are known as T2\* :

$$\frac{1}{T_2^*} = \frac{1}{T_2} + \frac{1}{T_2'} \quad (2.18)$$

Since T2 decays occur at different rates for different spins following the RF pulse, the TE is often a key parameter for resultant T2 contrast in MRI images. Up to the point of total signal loss due to dephasing, a longer TE results in more T2 contrast, or T2-weighting. Of course, T2 decay also occurs during the readout, but this effect is usually ignored.

### *Gradient echo and spin echo*

Most pulse sequences are based on gradient echo or spin echo techniques. In a gradient echo acquisition, spins are excited by a given flip angle and subsequently dephased and refocused by gradient-controlled encoding alone. In a spin echo, spins are excited with dual 90 and 180 pulses with a small time separation TE/2. The 180 pulse reverses the precession of the excited spins, resulting in the elimination of phase due to background magnetic field inhomogeneities at time TE following the 90. Regular gradient-controlled frequency encoding is made to coincide with this TE, so as to eliminate the contribution

of  $T2^*$  contrast (see Eq. 2.18) on the measured frequency-encoded data. In both gradient echo and spin echo techniques, the excitation and readout is repeated many times with different phase encoding steps to fill in the k-space grid line-by-line. Spin echo based sequences result in more pure  $T2$  contrast instead of  $T2^*$  contrast, at the expense of a longer TE and total scan time.

### *Scan time*

In standard 2D and 3D acquisitions, the total scan time is set by the total number of phase encoding steps times the TR. However, in many sequences, more than one phase encoding step is packed into a single TR (e.g. interleaved multi-slice, fast spin echo FSE, echo planar imaging EPI etc.), making the exact imaging time relationship more complicated, but a proportionality between total scan time and total number of phase encoding steps still holds.

## **2.2 Phased array RF receiver coils**

### **2.2.1 Volume coils vs. surface coils**

RF coils are key components of the MRI scanner, responsible for exciting spins and subsequently receiving their signals. RF coils can generally be classified into two categories: volume coils and surface coils.

A volume coil is a single large, usually cylindrical, coil that covers the entire imaging region, that is always designed for transmission and sometimes also for reception. By far the most common type of volume coil is the birdcage coil [10], which is shaped like a

birdcage or a ladder wrapped around a cylinder. A birdcage coil is a cylindrical coil that has sinusoidal current variation with polar angle when driven with a resonant RF signal at a single drive point [3]. This sinusoidal current distribution on the surface of a cylinder produces a very uniform linearly polarized magnetic field within the volume enclosed by the cylinder, resulting in uniform excitation and reception (through reciprocity) over the sample. The coil is always driven in quadrature (90 degrees apart) in space *and* time in order to produce a highly uniform circularly polarized RF field, which is maximally efficient for transmission since only fields which co-rotate with the spins can excite them [11].

A surface coil is a small receiver coil designed to image only a limited region. While some surface coils are used for both RF transmit and receive [12], the following discussion will focus on those used just for signal reception with relatively uniform excitation performed by a large volume resonator. While converting any transmit surface coil with to a T/R (transmit/receive) coil does not require any modifications to the coil, dedicated receive coils require special detuning electronics. A diode-containing trap circuit that is integrated into the coil matching circuit, and activated by a DC bias signal from the scanner, detunes the surface coil during volume transmit, protecting the sensitive scanner preamplifiers from the large transmit power, and preventing induced currents in the coil which may alter the transmit pattern [13].

Surface coils are very desirable for their high SNR, which they achieve because of more limited exposure to body noise, but they are limited in spatial coverage. However,

multiple surface coils can be arranged into a “phased array” in order to achieve the coverage of a single larger volume coil with the high SNR of a smaller surface coil [13]. When using phased array coils, a separate image is simultaneously acquired for each coil, and the data is combined to produce a high SNR final image. In most cases a uniform volume transmitter is paired with array reception. Also, phased array coils enable faster MRI scans through parallel imaging, as will be described in Sec 2.3.

### 2.2.2 Phased array image combination

Imaging with multiple coils implies that multiple images are collected for any slice. These images need to be combined into a composite image for each slice. For every pixel in the composite image, multi-coil imaging results in an over-determined system of equations that needs to be inverted to solve for that pixel’s  $M$ . Taking the example of four coils,

$$\begin{bmatrix} I_1 \\ I_2 \\ I_3 \\ I_4 \end{bmatrix} = \begin{bmatrix} S_1 \\ S_2 \\ S_3 \\ S_4 \end{bmatrix} M \quad (2.17)$$

where the  $I$ ’s are the individual coil pixel values collected and  $S$ ’s are the coil sensitivities (antenna patterns) at this position in space. This equation can be solved using least squares, with the result for any number of coils [13]

$$M = \frac{\sum_{n=1}^{N_{coils}} S_n I_n}{\sum_{n=1}^{N_{coils}} S_n S_n^*} \quad (2.18)$$

This expression requires detailed knowledge of the individual coil sensitivity maps. These maps can be obtained either through a separate sensitivity calibration scan, or by

analytic calculations based on exact knowledge of the coil positions in the field of view. Both of these techniques are cumbersome and prone to errors, so most frequently the above expression is approximated by taking the square root of the sum of squares of the individual coil image pixel values,

$$M = \sqrt{\sum_{n=1}^{N_{coils}} I_n I_n^*} \quad , \quad (2.19)$$

effectively using the individual coil images themselves as approximations to the coil sensitivity maps [13].

## **2.3 Parallel imaging techniques**

### **2.3.1 Overview**

Traditionally, faster MRI has been achieved with stronger and faster-switching gradients and faster receiver electronics, which allowed shorter intervals between data collection steps, and traversal of greater portions of k-space with each excitation [14]. However, these “fast” techniques continued to acquire data in a sequential manner. The recently developed techniques of parallel imaging allow the complex sensitivity profiles of the individual coils in a phased array to take over part of the spatial encoding normally performed exclusively by gradients in a sequential manner, thus saving time by eliminating some of these steps [15-17]. Parallel imaging techniques enable either a faster scan for a fixed matrix size (fixed resolution and coverage), or a larger matrix size (higher resolution and/or greater coverage) for a fixed scan time. This is in contrast to the conventional goal of phased array imaging, which is to improve SNR for a fixed matrix size and scan time.

The parallel imaging acceleration factor is known as the reduction factor  $R$ . For a typical array size of eight elements,  $R=2$  or  $3$  is typically practical. However, this technique can be limited by the reduction in SNR due to reduced signal averaging within the shorter imaging time, as well as by additional SNR losses that may occur due to difficulties in reconstructing undersampled data. Thus parallel imaging techniques are well suited to higher field strengths, where more baseline SNR is available. A variety of parallel imaging techniques exist, which operate in both the image and k-space domains.

### **2.3.2 SENSE**

Sensitivity encoding (SENSE) is a parallel imaging technique that is based in the image domain [16]. SENSE works by unfolding images that contain controlled aliasing as a result of discrete sampling, using known sensitivity profiles of the individual coils.

An explanation for SENSE requires a more detailed return to the discussion of MRI signal localization in Sec 2.1.5. The preceding basic discussion ignored the effects of discrete and finite sampling, since it was based on continuous Fourier transform analysis, which assumes that the entire k-space function is known. In reality, discrete and finite sampling of the k-space function set limitations on the MRI field of view and spatial resolution, respectively. The relationship between discrete sampling and field of view is exploited in SENSE. The discussion of the effect of finite sampling on spatial resolution is relevant to all MR imaging (not only SENSE), and is included for completeness on the topic of MRI sampling.

The operation of periodic discrete sampling of a continuous one-dimensional MRI signal  $s(k)$  is modeled by multiplication of  $s(k)$  with a “comb” function

$$u(k) = \sum_{p=-\infty}^{\infty} \delta(k - p\Delta k) \quad (2.20)$$

or infinite sum of evenly spaced Dirac delta functions with sampling interval  $\Delta k$  [4]. The acquisition of only a finite number of samples is modeled by multiplication of  $s(k)$  with a boxcar or rectangular wave “rect” function with dimension corresponding to the sampling window  $W$ . Combining both effects, the resulting product function  $s'(k)$  is

$$s'(k) = s(k) \cdot u(k) \cdot \text{rect}\left(\frac{k + \Delta k / 2}{W}\right), \quad (2.21)$$

assuming symmetric sampling of  $k$ -space defines the rect function.

The reconstructed spin density, or inverse Fourier transform of this product function, is

$$\begin{aligned} S'(x) &= \int_{-\infty}^{\infty} dk \sum_{p=-n}^{n-1} s(p\Delta k) \delta(k - p\Delta k) e^{2\pi j k x} \\ &= \sum_{p=-n}^{n-1} s(p\Delta k) e^{2\pi j p \Delta k x} \end{aligned} \quad (2.22)$$

for  $2n$  total evenly-spaced samples [4]. From this equation, the reconstructed spin density is periodic with period  $1/\Delta k$  as a result of discrete sampling. If an imaged object is larger than  $1/\Delta k$ , aliasing from points at multiples of  $1/\Delta k$  away must be present in the image. Thus the sampling interval  $\Delta k$  sets the field of view that is free from aliasing in conventional MRI.



Defining the spatial resolution in MRI is trickier. The spatial resolution is nominally defined as the field of view divided by the matrix size. In reality, finite sampling always results in some degree of blurring. Using the convolution theorem, (2.21) can be expressed in the image domain as

$$S'(x) = S(x) * U(x) * \left( W \operatorname{sinc}(\pi Wx) e^{-j\pi x \Delta k} \right) \quad (2.23)$$

where each term has been inverse Fourier transformed, and all products have been converted to convolutions [4]. This equation shows that sinc blurring occurs in all MRI images. But the degradation is minimal and FOV / matrix size is a reasonable measure of spatial resolution provided that the sampling window  $W$  is large enough, so that the sinc term approaches a Dirac delta function. In practice, this blurring or “ringing” is usually limited to regions of sharp signal transitions such as object edges, especially for a small object within a large FOV.

In SENSE, the  $\Delta k$  between phase encoding lines is deliberately set too large for the object, while  $W$  is held constant, resulting in a set of smaller, aliased coil images with identical resolution. Each aliased pixel in the undersampled individual coil images contains a superposition of the signals from  $R$  pixels separated by multiples of FOV/ $R$  in the true image space. For each aliased pixel,  $R$  true pixel values need to be separated. The theory of SENSE can be seen as an expanded version of the conventional phased array image combination theory presented in Sec 2.2.2. Extra columns ( $R-1$ ) are added to the encoding matrix in (2.17) that reflect the sensitivities of the aliased coils at the superposed pixel locations, and extra rows are added to the magnetization column to represent the unknown magnetizations at these locations. SENSE with  $R=1$  reduces to

standard combination. For example, for eight coils accelerated by a factor of two, the encoding equation for a given aliased pixel and its two superposed true pixels becomes

$$\begin{bmatrix} I_1 \\ I_2 \\ I_3 \\ I_4 \\ I_5 \\ I_6 \\ I_7 \\ I_8 \end{bmatrix} = \begin{bmatrix} S_{1,1} & S_{1,2} \\ S_{2,1} & S_{2,2} \\ S_{3,1} & S_{3,2} \\ S_{4,1} & S_{4,2} \\ S_{5,1} & S_{5,2} \\ S_{6,1} & S_{6,2} \\ S_{7,1} & S_{7,2} \\ S_{8,1} & S_{8,2} \end{bmatrix} \begin{bmatrix} M_1 \\ M_2 \end{bmatrix} \quad (2.24)$$

As long as the number of columns in the encoding matrix  $S$  (or reduction factor  $R$ ) is less than the number of coils, an over-determined system of equations is formed, which can be solved using linear algebra, in the same way as the conventional array combination equation. The general least squares solution is

$$\bar{M} = (\tilde{S}^H \tilde{S})^{-1} \tilde{S}^H \bar{I} \quad (2.25)$$

Simulated images for the eight coil,  $R=2$  case of SENSE imaging to illustrate the unaliasing procedure are presented in Fig 2.1. The simulated images and coil sensitivities were computed in Matlab through use of the Biot-Savart law (Sec 3.3.1), based on the geometry of an eight-coil receiver array with cylindrical symmetry. The simulated phantom is a cylinder imaged in cross-section.

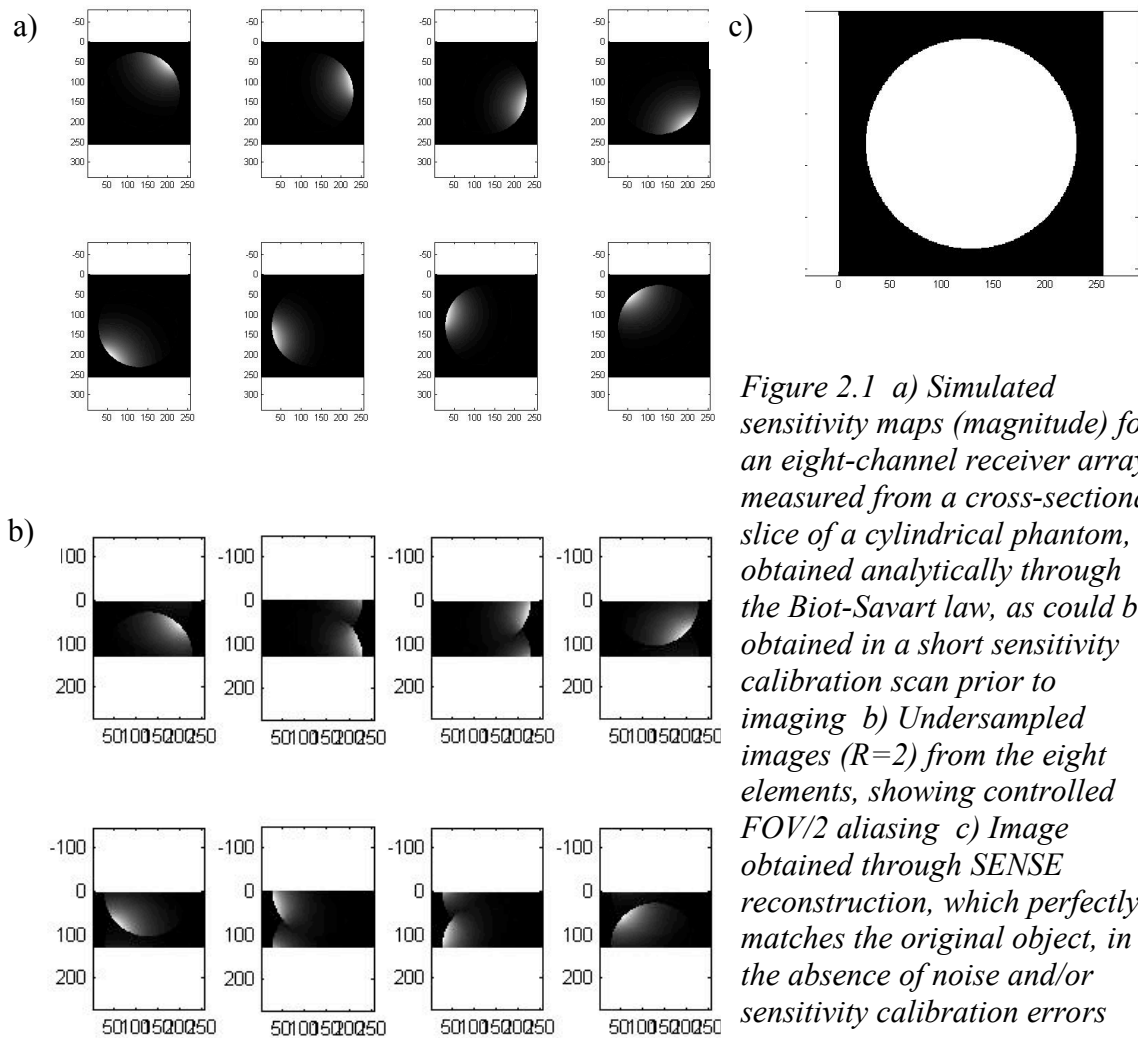


*Figure 2.1 a) Simulated sensitivity maps (magnitude) for an eight-channel receiver array, measured from a cross-sectional slice of a cylindrical phantom, obtained analytically through the Biot-Savart law, as could be obtained in a short sensitivity calibration scan prior to imaging b) Undersampled images ( $R=2$ ) from the eight elements, showing controlled FOV/2 aliasing c) Image obtained through SENSE reconstruction, which perfectly matches the original object, in the absence of noise and/or sensitivity calibration errors*

Application of SENSE reduces the scan time by a factor of  $R$ , but some extra time is required for a separate calibration scan to acquire the coil sensitivity maps. This can usually be accomplished in about 10 seconds through a low resolution, multi-slice gradient echo acquisition with proton density weighting (low flip angle, long TR, short

TE) to eliminate T1 and T2 effects on the sensitivity maps. Sensitivity calibration errors due to motion between calibration and the scan, contamination from tissue contrast, or other factors are a major problem in SENSE. The sensitivity maps are usually low-pass filtered and / or divided by a uniform coil image (ie. from the body coil) to help eliminate tissue contrast and otherwise eliminate the errors in these maps. Furthermore, the object must be masked as part of the reconstruction procedure to avoid the singular encoding matrices that are formed when one or more superposed pixels lie outside the object [18].

Acceleration using SENSE results in the degradation of image SNR by a factor of the denominator in the expression

$$SNR_{SENSE} = \frac{SNR_{full}}{g\sqrt{R}} \quad (2.26)$$

where  $g$  is the regionally dependent geometry factor

$$g = \sqrt{(S^H S)_{\rho,\rho}^{-1} (S^H S)_{\rho,\rho}} \geq 1 \quad (2.27)$$

and  $\rho$  is the index of the pixel within a set of superposed pixels under consideration [16]. The geometry factor is so named because of its dependence on array coil geometry, and rises quickly for higher reduction factors, resulting in prohibitive SNR losses at reduction factors approaching the number of coils.

The application of SENSE to single shot diffusion weighted echo planar imaging of the brain will be described in Sec 4.1.

### 2.3.3 SMASH

Developed in 1997 by Sodickson et al., simultaneous acquisition of spatial harmonics (SMASH) was the first practical parallel imaging technique [17]. SMASH attempts to mimic the spatial harmonics normally produced by gradients through linear combinations of coil sensitivity maps.

The signal equation (2.15) can be modified to include the effect of non-uniform coil sensitivity profiles  $C$ . Neighboring phase encoding lines in k-space are related by known spatial harmonic functions  $e^{jm\Delta ky}$  that are normally produced by sequential phase encoding gradient steps. If the function  $C$  is known, it is possible to construct a sum of individual coil signals from one acquired line to synthesize one or more composite neighboring lines. For a given spatial harmonic  $e^{jm\Delta ky}$ ,

$$\sum_{n=1}^{N_{coils}} a_{n,m} \int_x \int_y C_n(x,y) M(x,y) e^{-2\pi j [k_x(t)x + k_y(t)y]} dx dy = \int_x \int_y M(x,y) e^{-2\pi j [k_x(t)x + k_y(t)y]} e^{jm\Delta k_y y} dx dy \quad (2.28)$$

The coefficients  $a_{n,m}$  are determined by fitting the coil sensitivities  $C$  to the corresponding spatial harmonic functions.

$$\sum_{n=1}^{N_{coils}} a_{n,m} C_n(x,y) = e^{jm\Delta k_y y} \quad (2.29)$$

The acquisitions for SENSE and SMASH are exactly the same. SMASH is also based on uniform undersampling of phase encoding lines by a factor of  $R$ , as well as separate acquisition of sensitivity calibration maps. However, the reconstruction procedure is different, as SMASH proceeds through synthesis of missing lines in k-space through the fitting of  $R$  spatial harmonic functions.

SMASH forms the conceptual basis for generalized autocalibrating partially parallel acquisition (GRAPPA), which has superior performance to SMASH and other SMASH-like techniques [15]. Moreover, GRAPPA is autocalibrating, meaning that no separate sensitivity maps are required, in contrast to SENSE and SMASH. A GRAPPA reconstruction algorithm was developed as part of this thesis work for the purpose of acquiring and reconstructing cerebral MR angiographic data, the details of which will be described in Sec 6.2.2.

## ***2.4 Imaging of neurovascular disease***

### **2.4.1 Overview of neurovascular diseases**

Cerebrovascular disease is the third leading cause of death in the U.S. [19]. This is mainly attributable to stroke (loss of brain function due to interruption of blood supply), but it also encompasses a wide range of other pathologies, including intracranial aneurysms (arterial bulges which may hemorrhage), arteriovenous malformations (AVM, an abnormal collection of arteries and veins that shunt the capillaries), vascular abnormalities due to intracranial masses, fibromuscular dysplasia (a disease characterized by abnormal growth and development of vessel wall tissues, frequently resulting in spontaneous dissection of the internal carotid artery), vasculitis (inflammation of blood vessels), and vasospasm (blood vessel spasm, leading to vasoconstriction).

The principal cause of stroke, as well as many other vascular and cerebrovascular pathologies, is atherosclerosis [20]. Atherosclerosis is a degenerative disease characterized by the accumulation of plasma lipids, fibrous connective tissue, and cells in the tunica intima (innermost cell layer of cells) of blood vessels. This can result in the formation of hard plaques within the vessel, leading to stenosis (narrowing of the vessel lumen, or channel for blood flow), ulceration (erosion of the vessel wall tissue), thrombosis (clot formation), distal emboli (migration of a clot to another location, causing a blockage), and/or formation of fusiform aneurysms due to vessel enlargement.

#### **2.4.2 Catheter angiography**

Although its role is less frequently as a first imaging study, the gold standard technique for studying cerebrovascular disease remains conventional catheter angiography. This is a considerably invasive procedure, which involves puncturing the femoral artery and snaking a catheter up to the neck for iodinated contrast agent administration during imaging. Due to its invasiveness, even recent statistics indicate that catheter angiography carries a significant risk of neurologic complications (1.3%), with 0.5% experiencing permanent damage [21]. Furthermore, the procedure administers substantial iodinated contrast agent dose as well as ionizing radiation dose, is very expensive due to the equipment and personnel required (on the order of \$5,000-10,000), and is limited to 2D projection imaging.

The main advantage of catheter angiography, and the reason it maintains gold standard diagnostic status, is its excellent spatial and temporal resolution. Another key advantage is the ability to do simultaneous diagnostic imaging and image-guided treatment, since

endovascular coils and other treatment devices can be catheterized within the same procedure.

### **2.4.3 US / CTA / MRA**

For the reasons mentioned above, there is a tremendous demand for less invasive, safer alternatives to catheter angiography. The most important currently available options are ultrasound (US), computed tomography angiography (CTA), and magnetic resonance angiography (MRA), with or without contrast enhancement (CE).

#### *Ultrasound*

Ultrasound can be used to form images by measuring the distances to the characteristic acoustic impedance mismatches present at tissue interfaces. These distances are measured by sending ultrasonic pressure waves (frequencies  $\sim$  1-50 MHz) into the body and measuring the echoes that are produced. The main advantages of US are that it is inexpensive, portable, safe, and has excellent realtime capability (rivaled only by catheter angiography). However, it is much more limited than other techniques in spatial resolution and depth of coverage, especially when imaging through bone, such as the skull. These specifications suit it for imaging large vessels, near the skin surface (e.g. carotids in the neck). Using the Doppler frequency shift effect caused by bouncing sound waves on moving blood, US scanners can also generate dynamic maps of blood flow.

#### *CTA*

Computed tomography (CT) works by reconstructing a series of radiographic projections, in which signal is attenuated by elements with high atomic number (e.g. calcium in bone,



or iodine in contrast agent injected into the blood). Fast CT scanners (e.g. 64 detector row with 1/3s gantry rotation) allow intracranial arteriograms to be collected within the short arteriovenous transit time, with good spatial resolution (0.7mm in plane, 0.6mm through plane) [22]. Contrast is achieved through venous injection of iodinated contrast agent, which carries a small risk of kidney damage [23]. Also, a significant dose of ionizing radiation is administered, which presents a risk of radiation side-effects and is especially problematic in children [24, 25].

### *MRA*

Several MRA techniques have been developed for evaluation of the intracranial vasculature, including time-of-flight (TOF) MRA, phase contrast (PC) MRA, and contrast-enhanced (CE) MRA [26]. TOF MRA is based on flow related enhancement (FRE), and is capable of producing very high resolution arteriograms, as will be demonstrated later. However, it is vulnerable to “flow void” artifacts in regions of slow or unusual flow. PC MRA employs flow-encoding gradients to map blood motion onto image phase, producing images of blood velocity (magnitude and/or direction). CE MRA utilizes venous injection of gadolinium-based (Gd) contrast agents to shorten the T1 relaxation times of blood about ten-fold, producing images with very good contrast between blood and background tissues, and reduced vulnerability to flow voids. However, CE MRA techniques are limited in spatial (and temporal) resolution because of the limited number of sequential phase encoding steps that can be achieved during the imaging window, which is the first pass of the contrast agent (only a few seconds long). CE MRA techniques are also hampered by signal contamination from the venous phase.

Recent evidence indicates an association between gadolinium based contrast agents used in CE-MRA and nephrogenic systemic fibrosis (NSF) in patients with pre-existing renal disease [27-29], a severe complication of CE procedures, prompting the FDA to issue a recommendation to limit their use in these patients. This is an alarming disadvantage in the context of increasing prevalence of end stage renal disease (ESRD) [30].

### **3 Development of novel non-overlapping, capacitively decoupled phased array coils for conventional and parallel imaging**

#### **3.1 Overview**

An new eight-channel, non-overlapping phased array coil was designed and constructed for conventional MRI/MRSI and parallel imaging of the brain and the hip at 3 T [31]. The non-overlapping design was selected on the basis of reduced parallel reconstruction noise inflation, as predicted by the diminution of g-factor hotspots in SENSE reconstruction simulations, and the higher peripheral SNR expected from smaller coil elements. A novel capacitive bridging technique, modeled by a circuit simulation, was implemented to reduce the crosstalk between nearest neighbors to a manageable level. The capacitive decoupling technique was effective enough to allow the coil to be operated using standard system preamplifiers. In Chapter 4, studies are presented which demonstrate excellent coil performance in several conventional and parallel imaging applications.

#### **3.2 Motivation for non-overlapping design**

Higher SNR alone makes a case for coils with greater inter-element spacing than the conventional phased array overlapped to zero mutual inductance. For a fixed number of receiver elements arranged around a sample, an array with increased inter-element spacing (and thus smaller elements) certainly has regions of higher SNR, assuming body noise dominance is maintained. Also reduced next-nearest coupling would be provided

by these smaller, non-overlapping elements. Of course, beyond a certain point peripheral SNR is only gained at the expense of SNR in deep-lying regions. Nevertheless, this strategy would greatly benefit spectroscopic imaging studies of the cortical gray matter, for instance [32].

Additional motivation for our design comes from parallel imaging, which has introduced significant possibilities at high field for increased scan speed or increased scan coverage, as well as other application-specific advantages, such as the reduction of off-resonance artifacts and the improvements in SNR efficiency in diffusion-weighted single-shot EPI of the brain [33]. Parallel techniques are mainly limited by SNR losses that depend in large part on receiver coil design parameters, thus presenting new design criteria for RF coils. To take full advantage of parallel techniques, baseline SNR must be maximized, and reconstruction-related losses must be minimized (eg. the g-factor in SENSE [16]). Baseline SNR can be increased by reducing the receiver coil size (at least regionally, with the caveat mentioned earlier regarding SNR at deep regions), and reconstruction-related losses can be reduced by increasing the spacing between elements, thus providing sensitivity maps more diverse in magnitude and phase throughout the sample [34].

However, positioning coils in such configurations while maintaining good coverage between elements typically results in substantial mutual inductance between nearest neighbors, introducing the need for special decoupling techniques to reduce crosstalk between elements. Here I describe a new eight-channel, non-overlapping phased array

coil for 3 T that achieves decoupling through inter-coil capacitive networks, requiring only standard system preamplifiers.

### 3.3 Non-overlapping coil design

#### 3.3.1 SENSE simulations for optimizing coil geometry

Prior to coil construction, I investigated the dependence of extra SNR losses (beyond that due to scan time reduction) on coil geometry using SENSE reconstruction simulations.

The simulations were based on a quasi-static (low frequency) EM model which I programmed in Matlab, equivalent to those used in previous studies [35, 36]. Using this model, relative SNR maps can be calculated based the coil / sample geometric arrangement. A relative SNR map can be calculated using

$$SNR_{voxel} \propto \sqrt{S^H \Psi^{-1} S} \quad (3.1)$$

where S is the signal at the given voxel, and psi is the noise matrix

$$\Psi_{ij} = \int_{sample} E_i \cdot E_j^* dV \quad (3.2)$$

The signal at a given voxel is proportional to the transverse magnetic field produced per hypothetical unit current in the receiver coil (due to the principle of reciprocity described in Sec 2.1.4). In the low frequency regime, the transverse magnetic field can be computed through integration of the law of Biot and Savart over the receiver current loop

$$B_{\perp} = \left| \int_{coil} \frac{\mu_0 I d\vec{l} \times \hat{r}}{4\pi r^2} \right|_{\perp} \quad (3.3)$$

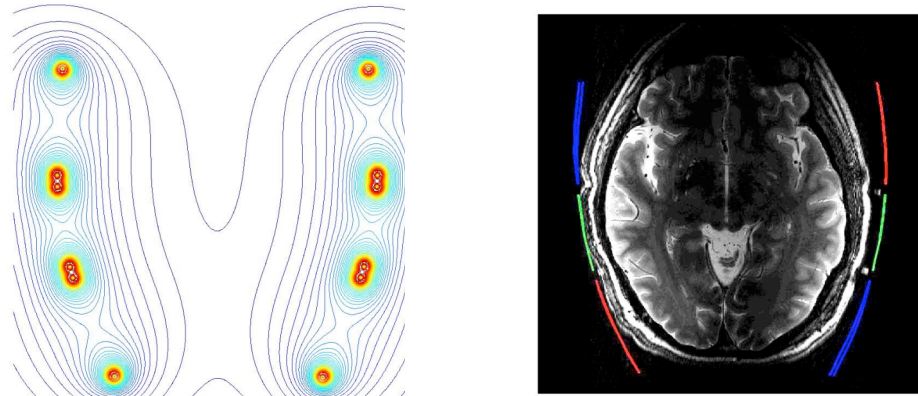


*Figure 3.1 Transverse magnetic field contour map (left) computed by the Biot Savart law, for a receive array of six elements aligned to the actual positions of the coils in an imaging experiment. The image (right) shows intensity variation due to the variation of the magnetic field across the head.*

where  $\mu_0$ =free space permittivity,  $I$ =unit current,  $dl$  is the differential line segment along the loop,  $r$  is the source to test point distance, and  $\hat{r}$  is the unit vector pointing between the source and test points [6]. A calculated contour plot of the magnetic field of an eight-channel array, and an actual image from the array are given below the formula. The standard deviation of the noise in a given coil is proportional to the square of the electric field produced at a given location due to the same hypothetical unit current, which is calculated through the magnetic vector potential [6]. This model is strictly valid only for low frequencies, and begins to break down in MRI at around 3Tesla (especially

when imaging large samples) due to interactions between the RF fields and the sample known as “dielectric effects” [24].

Since dielectric effects were ignored, the simulations were not intended to provide exactly optimized results at 3 T. Rather, they served as a source of general design guidelines regarding approximate expected SNR losses in SENSE reconstruction.

Volumetric g-factor maps were generated for left-right (LR) and anterior-posterior (AP) accelerations (up to rate-3) for a linear array of eight rectangular elements in a dual paddle configuration, arranged around a cylindrical phantom (elongated along the AP direction to simulate the shape of a head) of the same length as the coils. The coil widths and overlaps were varied, with no constraints concerning mutual inductance.

### **3.3.2 Construction**

Eight rectangular receiver loops were mounted, four per side, into bilateral plastic paddles curved to conform approximately to the shape of the head (right and left sides) or the hip (anterior and posterior sides of a single hip). The loop dimensions were 4.0 cm wide by 10.0 cm long, with a 1.7 cm inter-element gap (Fig. 3.2).

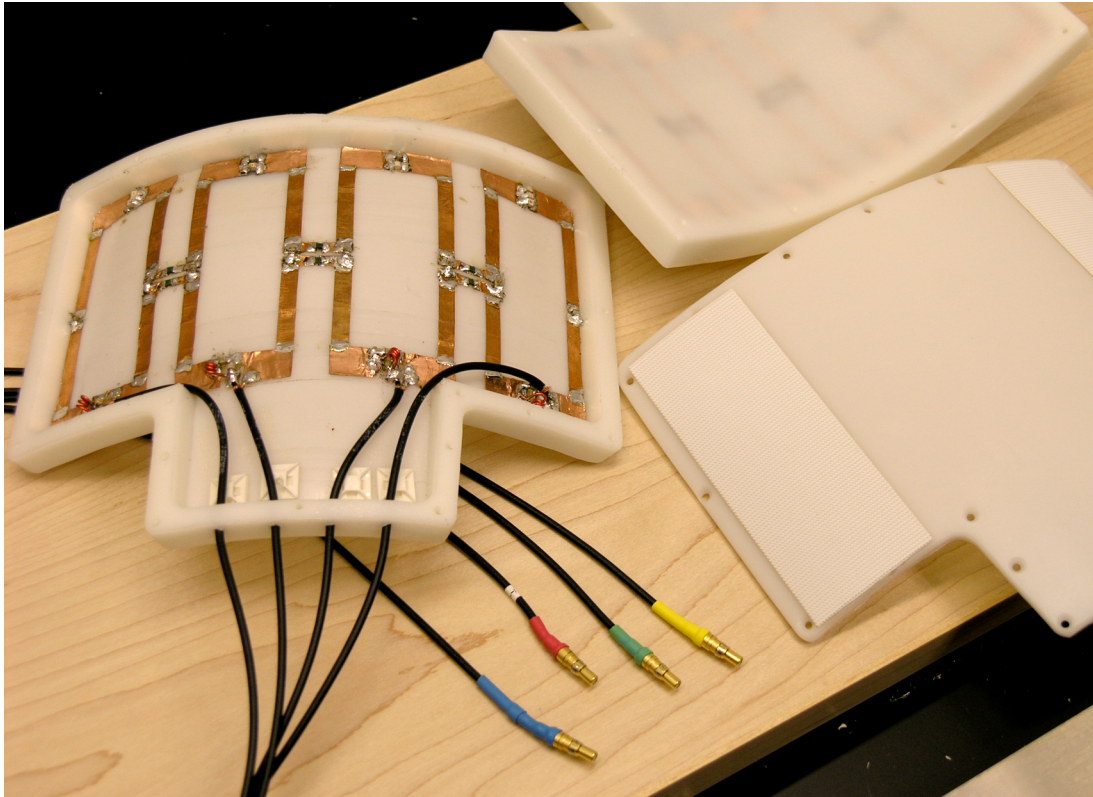


*Figure 3.2. Dual paddles comprising the eight-channel non-overlapping phased array coil, with outer cover of one paddle removed, showing receiver loops, trap detuning circuits, and transmission line cabling and connectors. Velcro fasteners affixed to the outer cover allowed good coil placement for head and hip applications.*

### **3.3.3 Tuning and matching**

The main electrical requirements for an RF receiver coil are tuning (and detuning) and impedance matching. Tuning and impedance matching are inseparable procedures that are necessary in order to be able to transfer power from the receiver coil through the cables to the amplifier and allow the scanner to receive NMR signals. Impedance  $Z$  is the



key network parameter for an RF circuit [6]. It is a complex number that relates the complex current (I) and voltage (V) in an RF circuit by

$$V = IZ \quad (3.4)$$

In order to transfer power from the receive coil to the cables, the receive coil impedance must match the cable characteristic impedance (50 ohms). The fraction of the received power that is transferred is

$$\Gamma = 1 - \left| \frac{50\Omega - Z_{coil}}{50\Omega + Z_{coil}} \right|^2 \quad (3.5)$$

The conducting loop of an RF coil is primarily inductive and thus has mostly complex impedance  $j\omega L$  (from the definition of inductance  $V=L \, dI/dt$  put into complex form). To transform this impedance to a purely real 50 ohms, the complex impedance is resonated out with series tuning capacitors with equal and opposite impedance ( $1/j\omega C = j\omega L$ ), and the leftover impedance is matched to 50 ohms using a matching circuit usually consisting of both series and shunt elements [13].

Receive coils must also detune (or equivalently, become mismatched) any time the transmit coil is on, to eliminate induced currents in the receive coils that may alter the transmit field, as well as to protect the receiver electronics. This was accomplished using a switched circuit that ensures a mismatch during transmit, physically realized by a diode-containing trap circuit that is activated by a DC signal from the scanner.

The quality of matching is usually measured through scattering parameters (S-parameters), which have a one-to-one relationship with impedances. Scattering parameters (or S-parameters) are based on the concept of a reflection coefficient, which is

easier to measure than actual currents and voltages at high frequencies [37].  $S_{11}$  in decibels (dB) is related to the coil impedance by

$$S_{11} = -20 \log_{10} \left( \frac{50\Omega - Z_{coil}}{50\Omega + Z_{coil}} \right) \quad (3.6)$$

and is also known as the return loss.

### 3.3.4 Decoupling

Mutual inductance between neighboring receiver coils results in crosstalk between receive channels, so coils need to be decoupled. Mutual inductance is time varying magnetic flux through one coil due to a time varying current in another coil, resulting in an induced voltage in the first coil [6]

$$M_{ab} = M_{ba} = j\omega \int_a \vec{B}_b \cdot d\vec{s}_a \quad (3.7)$$

Mutual inductance results in phase sensitive combination of coil signals, producing spurious cancellations and additions of signals in the individual receiver coils, resulting in artifacts [38]. Using this theory, I programmed computer simulations of the appearance of the coupling artifacts, based on Biot-Savart simulation of the receive profiles and estimation of the coupling factor due to mutual inductance, and found the results to be in good agreement with experimental data that was collected from a three-channel array (see Fig 3.3).

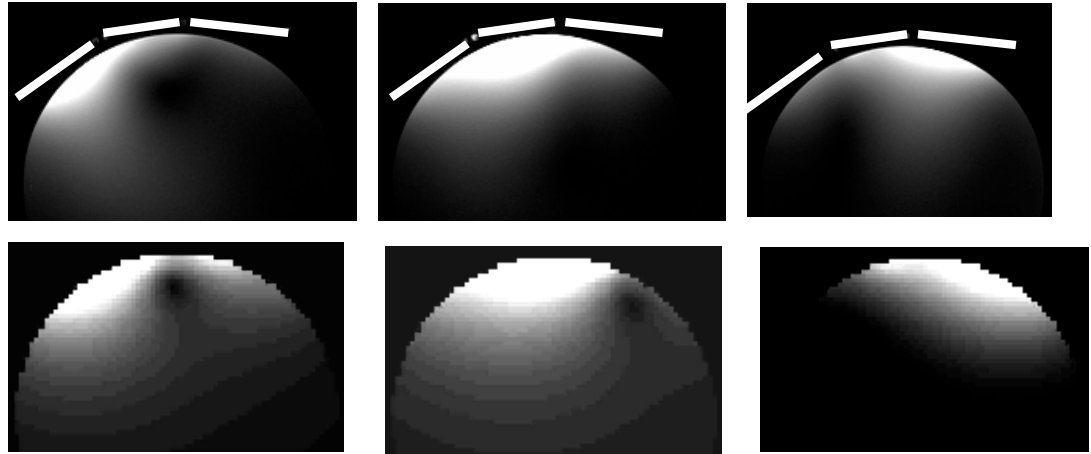


*Figure 3.3 - Top row: Experimental coil images from three-channel array coil with a small amount of residual coupling, bottom row: Simulated images generated through computer simulations based on the coil coupling theory presented by Tropp et al.*

Traditionally, adjacent receiver coils are overlapped such that flux through the overlapped region is exactly cancelled by oppositely-directed flux in the separated region, resulting in nearly zero net mutual inductance. In this case, the non-overlapping geometry resulted in significant mutual inductance, displaying an approximate coupling constant of  $k_m = .047$  as defined by Roemer et al. [13]. To counteract this, decoupling capacitance was installed between adjacent loops.

Based on the good agreement between the above simulations and experiments, I applied a novel RF circuit model to determine the capacitor values needed to decouple the coils, while maintaining the mandatory tuning and matching conditions. All of the nearest

neighbor relations present in each four-element linear array are also found in a three-element array. Therefore, a three-receiver (five-loop) Kirchoff mesh currents circuit model was used to predict the correct capacitor values required to decouple the coils. Neglecting interactions beyond nearest neighbors is especially reasonable in the non-overlapping geometry, since next-nearest neighbors are farther apart in this configuration. Parasitic self and mutual inductances of the loops formed by the decoupling capacitors were also neglected. This is reasonable since these loops were kept very small in the final implementation.

Impedance is generalized into a matrix form  $\tilde{Z}$  for a collection of circuits (i.e. an array coil). It gives the relationships between voltages and currents according to

$$\vec{V} = \vec{I}\tilde{Z} \quad (3.8)$$

where V and I are complex vectors of voltages and currents measured at various predefined points in a circuit. The impedance matrix for the capacitively decoupled three-coil phased array is given below (Figure 3.4a), along with the corresponding circuit diagram identifying the mesh currents (Figure 3.4b). The off-diagonal terms in this matrix are due to the mutual inductance and the presence of the decoupling capacitors.

$$\begin{bmatrix} j\omega L + \frac{1}{j\omega C_1} + \frac{1}{j\omega C_2} + \frac{1}{j\omega C_3} + \frac{1}{j\omega C_4} & \frac{-1}{j\omega C_4} & j\omega M & 0 & 0 \\ \frac{-1}{j\omega C_4} & \frac{1}{j\omega C_4} + \frac{1}{j\omega C_5} + \frac{1}{j\omega C_7} & \frac{-1}{j\omega C_7} & 0 & 0 \\ j\omega M & \frac{-1}{j\omega C_7} & j\omega L + \frac{1}{j\omega C_6} + \frac{1}{j\omega C_7} + \frac{1}{j\omega C_8} + \frac{1}{j\omega C_9} & \frac{-1}{j\omega C_9} & j\omega M \\ 0 & 0 & \frac{-1}{j\omega C_9} & \frac{1}{j\omega C_9} + \frac{1}{j\omega C_5} + \frac{1}{j\omega C_4} & \frac{-1}{j\omega C_4} \\ 0 & 0 & j\omega M & \frac{-1}{j\omega C_4} & j\omega L + \frac{1}{j\omega C_3} + \frac{1}{j\omega C_4} + \frac{1}{j\omega C_1} + \frac{1}{j\omega C_2} \end{bmatrix}$$

Figure 3.4a. Mesh impedance matrix for three-channel non-overlapping phased array,

with off-diagonal terms representing effects of mutual inductance and capacitive decoupling networks

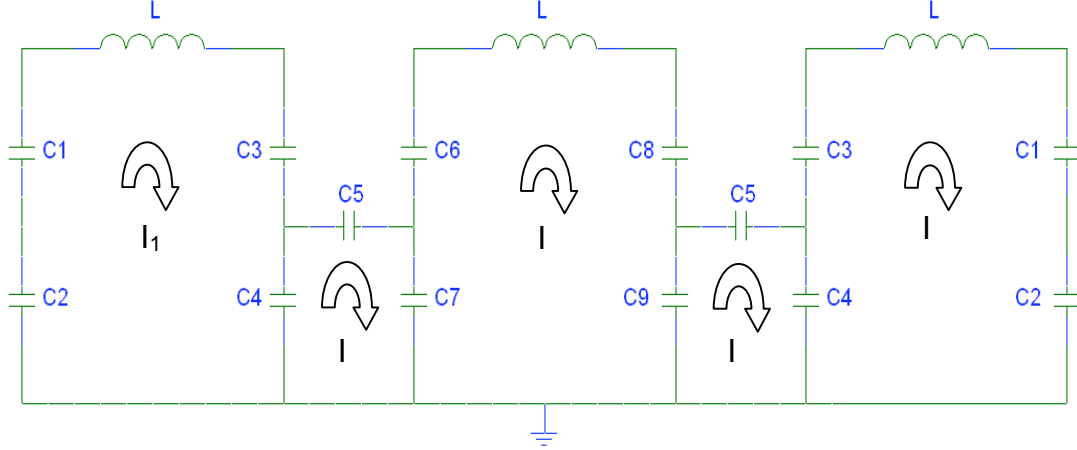


Figure 2b. Schematic for three-channel non-overlapping phased array, describing terms in above circuit model

At resonance,

$$\tilde{Z}\bar{I} = 0, \quad (3.9)$$

where  $\bar{I}$  is a column vector of non-trivial mesh currents  $I_1 - I_5$ . Separating the inductive and capacitive contributions to  $\tilde{Z}$  into  $\tilde{L}$  and  $\tilde{C}$  (i.e.  $\tilde{Z} = \tilde{L} + \tilde{C}$ ), and factoring out constants, this can be rewritten as

$$-\omega^2 \tilde{L}\bar{I} = \tilde{C}\bar{I}. \quad (3.10)$$

$\tilde{L}$  and  $\tilde{C}$  consist of bench-derived knowns (except for  $C_5$ ), and the value of  $C_5$  was iterated until three of the eigenvalues  $\omega/2\pi$  were aligned at 127.7 MHz. Alignment of the eigenvalues corresponds to perfect isolation of the individual coils. The values of the

model parameters were  $L = 125$  nH,  $M \approx k_m L = 5.9$  nH,  $C_{1-4,7,9} = 47.5$  pF, and  $C_{6,8} = 43.5$  pF.

### 3.3.5 Preamplifier and transmission line (T-line) considerations

Decoupling can be further improved through the use of special ultra-low impedance preamplifiers [13]. However, it is important to be aware of impedance transformation that occurs when the coils are connected to these amplifiers by T-line cabling that is a significant fraction of the wavelength. If the impedance is improperly transformed, coupling can actually be increased. The resulting impedance is

$$Z = 50\Omega \frac{Z_{amp} + 50j\Omega \tan(2\pi l / \lambda)}{50\Omega + jZ_{amp} \tan(2\pi l / \lambda)} \quad (3.11)$$

where  $l$  is the length of transmission line cable and  $\lambda$  is the wavelength in the T-line [6, 37]. To further minimize the effect of reactive coupling using the system's low impedance preamplifiers, the  $50 \Omega$  coaxial connection lengths were set to approximately one wavelength (a half-wave multiple which was convenient in practice for reaching the hip) to ensure low impedance is maintained.

Using a calibrated network analyzer directly connected to the RF receive inputs of the scanner, I made direct measurements of the reflection coefficient phase angles at the inputs to the scanner's preamplifiers (biased on) in order to calculate the exact cable lengths required, since details of the RF amplifier specifications were not otherwise available to me. To avoid any possible harmful exposure of the network analyzer to DC signal from the scanner, I added a series blocking capacitor (10pF) to the measurement

cable, prior to calibration. The results of the measurement are shown below, for one preamp.

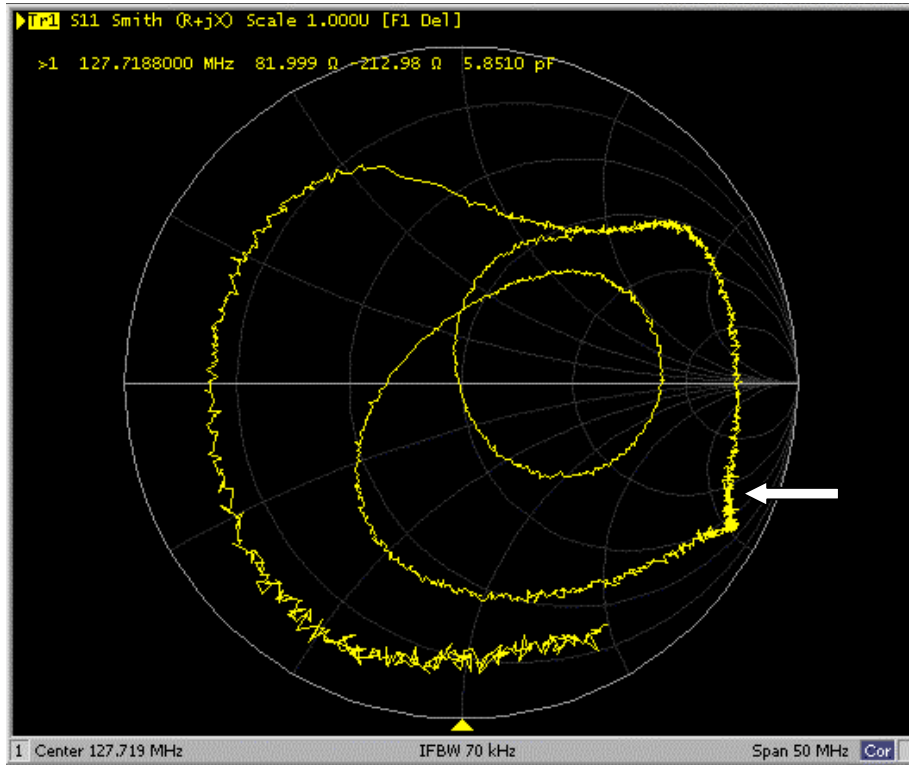


*Figure 3.5 – Smith chart polar plot of preamplifier reflection coefficient  $S_{11}$  in complex plane, with phase angle  $117^\circ$  (white arrow) from ideal short circuit (low) impedance @ 127.7 MHz, which was used to calibrate cable line lengths required for maximum decoupling*

### 3.4 Results

#### 3.4.1 SENSE simulations

As expected, the general result of the SENSE simulations that I performed was that candidate arrays with increased inter-coil spacing showed a marked reduction in the appearance of g-factor “hotspots” versus a comparable design having the same total spatial extent but overlapped to approximately zero mutual inductance. For example, for rate-3 SENSE in the RL direction using one non-overlapping design, the average g-factor over the sample dropped to 1.15 from 1.24 for an equivalent design overlapped to zero mutual inductance, and the peak g-factor was reduced to 1.49 from 1.85 (fig. 3). The result for AP acceleration was similar. I used the approximate dimensions of this particular array for fabrication.

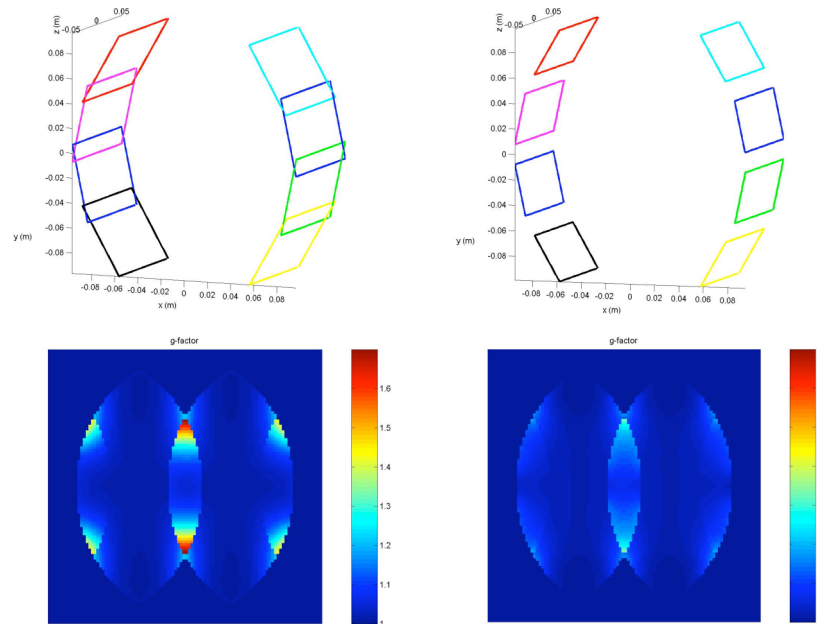


Figure 3.6 Coil schematics (top row) and g-factor maps (bottom row) for comparable overlapping (left column) and non-overlapping (right column) designs (coil length =



10.0cm, overlapping width=6.1cm, non-overlapping width=4.1 cm, phantom minor axis =12 cm, major axis=16cm)

### 3.4.2 Decoupling

My circuit model predicted that a capacitance of 13.7 pF would be required to decouple the coils. In practice, I determined that a series pair of 20 pF capacitors gave the best performance (placed around a tuning capacitor, as shown in the schematic below and in the photograph in Figure 3.2 above).

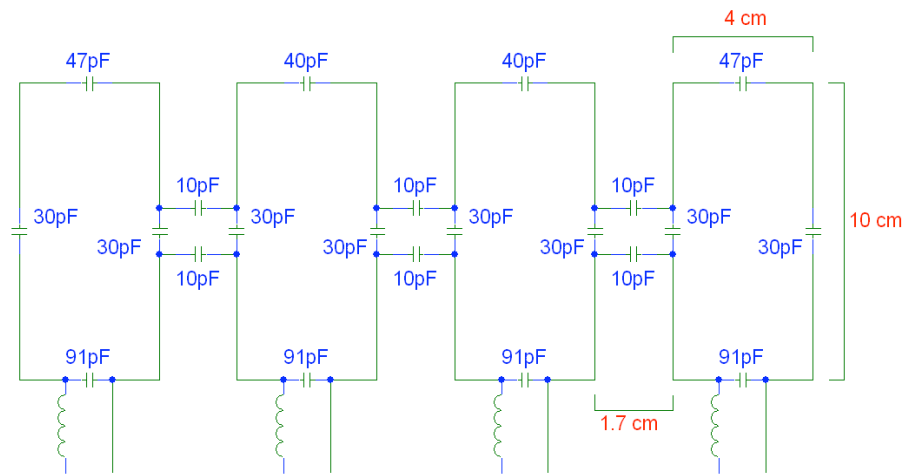
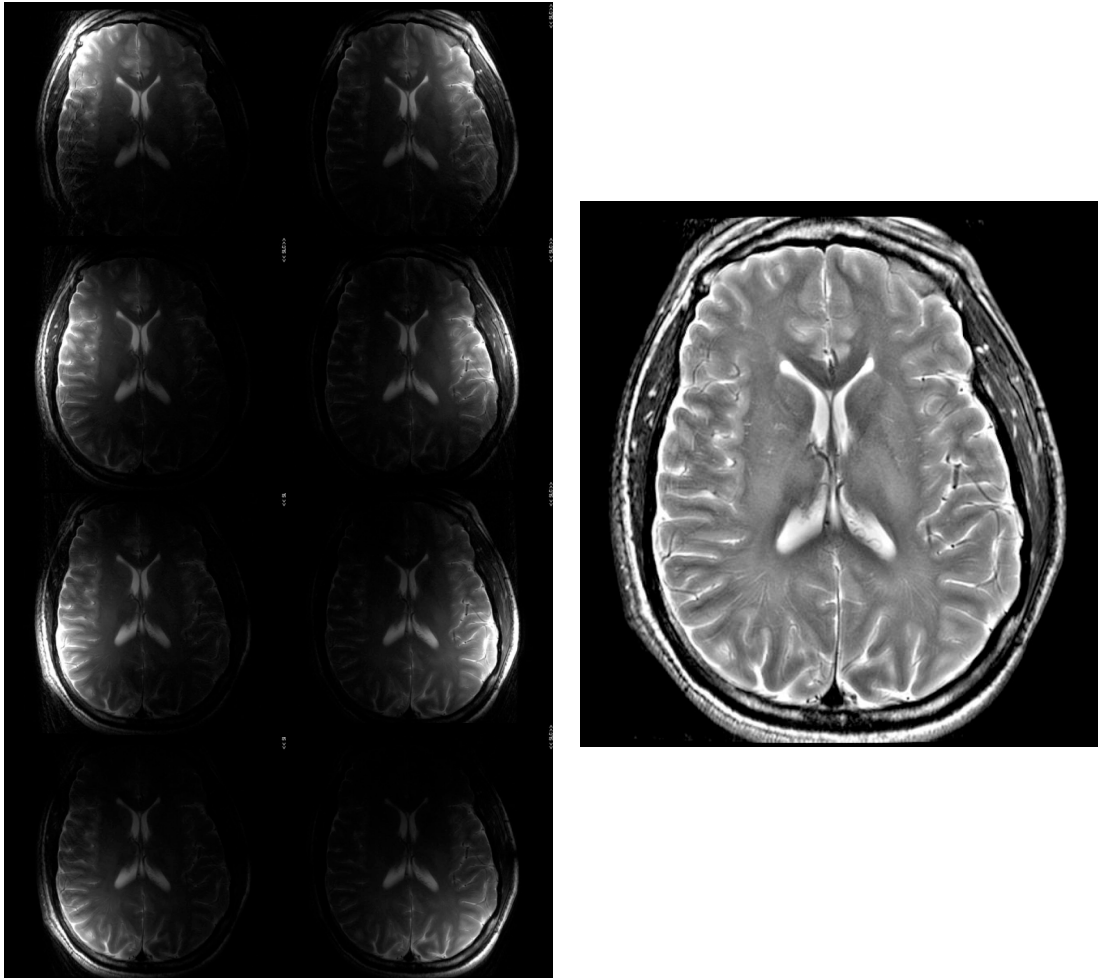


Figure 3.7 Schematic of non-overlapping array, showing final capacitor values implemented in the array, as well as coil dimensions and spacing

In this manner, the crosstalk that I measured on the network analyzer was reduced to a maximum of -14.0 dB (loaded  $|S_{21}|$ ) between nearest neighbors, and -25.0 dB for next-nearest neighbors, while maintaining an input match of better than -15.0 dB (loaded  $|S_{11}|$ ) on all coils. Anatomical images from the individual coils showed negligible signs of inter-element reactive coupling (fig. 4).



*Figure 3.8 Individual coil images (left) from an axial FSE scan with identical window-leveling (scan time  $\sim 3.5$  min,  $TR = 4$  s,  $TE = 103$  ms,  $NEX = 3$ ,  $384 \times 384$ ,  $FOV = 20$  cm, 8 slices, slice thickness = 5 mm, train length = 24), alongside sum of squares combined image (right) with filtering to remove coil sensitivity roll-off*

### **3.5 Discussion**

In this study I developed a novel curved eight-channel array for high resolution MR of the brain and hip. The final design criteria were chosen to strike a reasonable balance between the distinct demands of conventional and parallel imaging, despite substantial experimental variation. The predicted improvements in g-factors for smaller coils at various acceleration factors along both directions were balanced against the accompanying SNR loss at depth for conventional imaging. Differences in sample size, shape, and electrical properties introduce further variation.

The capacitive decoupling networks proved to be highly effective and convenient for decoupling phased array coils, in agreement with reports by previous investigators in high-field NMR microscopy [39]. The networks yielded enough isolation for the coil to be operated using standard system preamps. The proposed circuit model reasonably modeled their behavior, with an error of 37% on the predicted values. Possible sources of error include the lossless nature of the model, the parasitic self-inductances of the capacitive networks, and the general breakdown of lumped element analysis at the 3 T frequency of 128MHz.

### **3.6 Conclusions**

A new eight-channel, non-overlapping phased array coil was designed and constructed for both conventional and parallel imaging applications in the head and the hip at 3 T. I also have developed useful phased array coil simulation tools to aid in coil design, consisting of a numerical SENSE reconstruction simulation tools and a circuit model for

capacitive decoupling. The simulation tools and the experience in fabricating these coils should continue to be useful in the future development of larger arrays capable of larger reduction factors.

### ***3.7 Non-overlapping phased array coil for a MRI-compatible neonatal incubator***

#### **3.7.1 Background**

MRI techniques (including MRSI and DWI) have proven to be valuable tools for studying the developing pediatric brain. Metabolite levels from MRSI can be used to detect brain injury [40] and several inborn errors of metabolism [41-43]. MRSI can detect cellular metabolite changes that reflect anatomic variation and developmental maturation [44]. Information from DWI images about the magnitude and directionality of water diffusion has been applied in diagnosing acute ischemia [45], and DTI can be used to study the normal and abnormal developmental changes in white matter pathways [46].

#### **3.7.2 Purpose**

The purpose of this project was to design a dedicated eight-channel receiver coil array for a MRI-compatible neonatal incubator [47]. The design criteria were to achieve substantially higher signal-to-noise ratios (SNR) (at least peripherally) than other coils currently being used for scanning neonates, and enable parallel imaging for faster scans at the same resolution, and provide critical artifact reduction. Due to the anatomic variation of metabolite levels, it is important to obtain high spatial resolution spectra in order to avoid partial volume effects. More SNR is also needed in DWI to improve the spatial resolution and measurement certainty, in order to show fiber crossings more clearly in HARDI, for example. The need to freeze bulk motion and probe many diffusion

directions necessitates the use of fast sequences like single-shot EPI, which is strongly affected by magnetic field inhomogeneities and T2\* decay, but greatly improved using parallel imaging. Current state-of-the-art adult diffusion MRI system utilize parallel imaging acquisitions and a goal of this new RF coil design project is to bring this important capability to neonatal MRI studies.

### 3.7.3 Design constraints

First and foremost, certain design features of the coil are mandated by practical concerns. These include extra space between the baby and the coil and recessed endrings for easier longitudinal access and tubing pass-through (including ventilator, temperature monitor, O2 saturation monitor, IV, HR monitor, etc.). We propose to use a non-overlapping design in order to maximize radial access area while using small receiver coils. We are also constrained to use a design with 0° axial rotation, in order to allow direct vertical access for intubation. Fortunately, this is the preferred orientation for acceleration along the standard x - y directions anyhow.

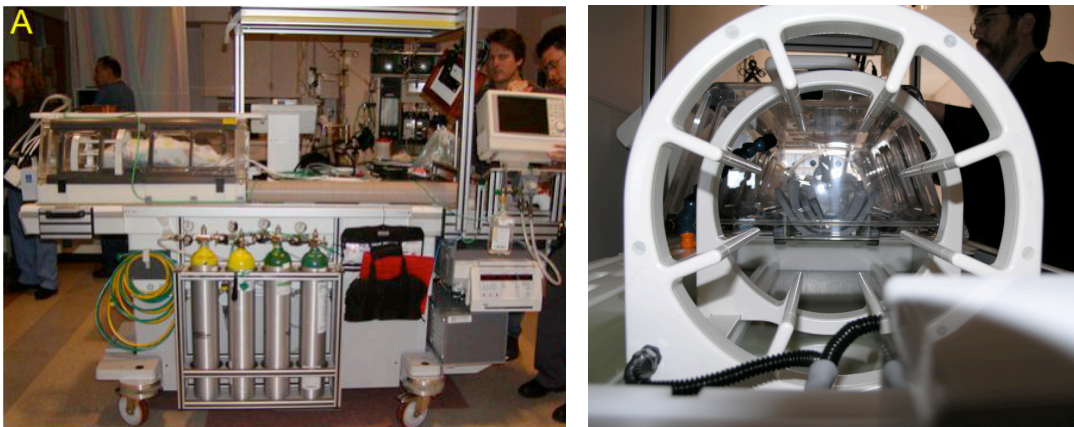


*Fig 3.9 – MRI-compatible neonatal incubator (left) and end-view of insert birdcage RF coil (right)*

### 3.7.4 Design optimization

Aside from these design constraints, the primary design goals are SNR and parallel imaging performance. Both of these purposes require going to more receivers. Using more receivers decreases the individual coil size and increases the SNR, and it also allows the more distinct individual coil profiles to take over more of the imaging process (i.e. higher acceleration factors). However, though additional receivers would likely be superior (up to a point), this design was limited to eight by the practical concern of radial access.

The remaining variable design parameters are related to coil size. In numerical simulations, I varied the width, length, overlap, and radius of the coils, as well as the sample dimensions, in order to determine the optimal geometry, over the range of parameters shown below. I selected the design shown in Figure 3.10, with specifications as described.

Table 3.1 - Ranges of coil design simulation parameters

	<b>coil length</b>	<b>overlap</b>	<b>d-inner</b>	<b>d-outer</b>	<b>sample min-axis</b>	<b>maj-axis</b>
<b>Range</b>	<b>10–20 cm</b>	<b>-3 - 3 cm</b>	<b>16-24 cm</b>	<b>20–32 cm</b>	<b>6-10 cm</b>	<b>8–12 cm</b>

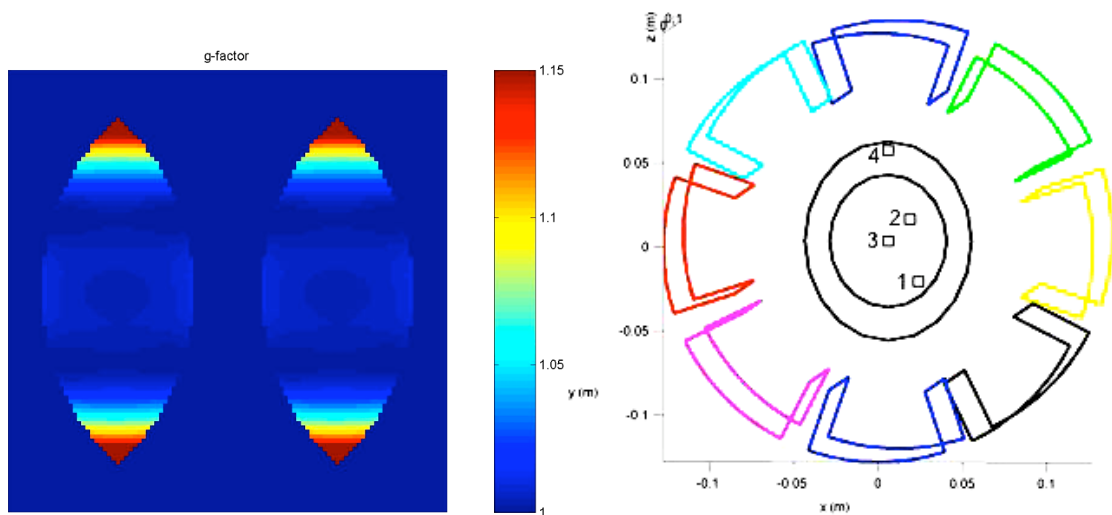


*Figure 3.10: Left: G-factor map for proposed neonatal coil with  $R = 2$  along  $x$ . Right: Proposed coil geometry used in simulations of coil performance, showing two elliptical neonatal head shapes with ROI's for SNR calculations inside*

Figure 3.10 shows a g-factor plot for mid-axial parallel imaging of a sample neonatal head using the proposed neonatal phased array coil, with rate-2 acceleration along the x(RL)-direction. The g-factor reflects the additional SNR penalty (beyond scan time reduction) associated with de-aliasing images with missing phase encodes, as compared to a fully encoded scan. The g-factor is shown to be very low ( $< 1.05$ ) throughout most of the FOV (except for some peripheral hot spots where  $g \sim 1.15$  (ie 15% loss)), meaning that minimal SNR is sacrificed overall. The dimensions of the ellipse representing the neonatal head were 7 cm wide by 8 cm high. On the right side of Figure 3.10, the ROI's for SNR calculations based on the proposed coil are shown. The expected SNR

performance for the proposed 8-channel neonatal phased array coil were calculated as described above and compared to those for the commercial 8-channel head coil for a smaller, preterm head (8x7cm) and a larger (12x10) size similar to that of a larger term infant. The calculated SNR increases were: for the smaller head ROI#1 = 49%, ROI#2=45%, ROI#3=43%; and for the larger theoretical head size ROI #4=45%. While the SNR increases will vary due to head size and require optimal construction, these simulations indicate that this coil will provide parallel imaging capability and an SNR improvement of 40-50% over the commercial 8-channel head coil. Also the phased array coil is expected to provide a 20-40% increase over the current neonatal recessed ring birdcage.



## 4 Clinical applications of the novel eight-channel nonoverlapping receive coil

### 4.1 Overview

I conducted conventional, spectroscopic, and parallel imaging studies of the brains and hips of normal volunteers demonstrate the good performance of the non-overlapping coil design. SNR improvements over a commercial eight-channel head coil were demonstrated in important structures in EPI-SENSE diffusion-weighted imaging. High resolution MRSI (0.22 cc) yielded SNR of up to 21 for the NAA peak in the cortical gray matter. The coil also provided excellent four-fold accelerated GRAPPA images of the hip. The good SNR values for a variety of applications (both conventional and parallel) demonstrated that a robust design was achieved.

### 4.2 Parallel diffusion weighted imaging (DWI) of the brain

#### 4.2.1 DWI background

Unrestricted diffusion is characterized by the equation:

$$r_{rms} = \sqrt{2Dt} \quad (4.1)$$

where  $r_{rms}$  is the root-mean-square displacement,  $D$  is the diffusion coefficient ( $\text{mm}^2/\text{s}$ ), and  $t$  is time [48]. Diffusion of water in tissues is obstructed to varying degrees and possibly also in a directionally-dependent manner by the presence of macromolecules and cellular structures. In DWI, a bipolar gradient with large and equal but opposite lobes (of duration  $\sim 50\text{ms}$  @ max. gradient amplitude) applied prior to readout results in signal loss due to intravoxel dephasing. The MRI signal is attenuated according to

$$S = S_0 e^{-bD} \quad (4.2)$$

where  $D$  is the diffusion coefficient along the given diffusion gradient direction [48]. The  $b$ -value ( $\sim 500$ - $1000 \text{ s/mm}^2$  for brain) depends mainly on the shape of the diffusion gradients and quantifies the degree of sensitization of the imaging experiment to diffusion, or the degree of diffusion weighting. To generate orientation-independent images, the geometric mean of three DW images is taken, each with diffusion gradients along an orthogonal direction. If quantitative data is desired,  $S_0$  can be determined using a  $b=0$  acquisition, and the above equation can be solved for  $D$ , which is actually known in DWI as the apparent diffusion coefficient (ADC), since other effects such as bulk motion can influence the measured value of  $D$ . The primary clinical application of DWI has been in early detection of cerebral ischemia [49]. When the anisotropy of diffusion is important, such as in white matter fiber tracts in the brain, the elements of the diffusion tensor can be determined using diffusion tensor imaging (DTI) [50].

DWI is most commonly implemented as single shot echo planar imaging (ss-EPI), since this technique images quickly and limits the sensitization to bulk motion. In ss-EPI, an entire 2D image is formed in each TR interval ( $\sim 150 \text{ ms}$ ), using oscillating readout gradients separated by orthogonal phase encoding gradient pulses. ss-EPI techniques are largely limited by poor spatial resolution (typically  $128 \times 128$ ) because of susceptibility-induced signal dropouts and geometric distortions due to the  $T_2^*$  dephasing that occurs by the middle of longer readouts. The middle of the readout is the “effective TE”, and is much longer than typical gradient echo TE’s. ss-EPI sequences benefit greatly from parallel encoding, which reduces the effective TE while maintaining the spatial

resolution, resulting in less T2\* blurring, signal dropouts, and geometric distortions [33, 51].

#### 4.2.2 Parallel DWI human studies using ssEPI-SENSE

I acquired ssEPI DWI images using the prototype coil with and without SENSE. Sample results from the same slice in the same volunteer are shown below. A reduction of susceptibility-induced signal dropout and T2 blurring is evident when using parallel imaging.

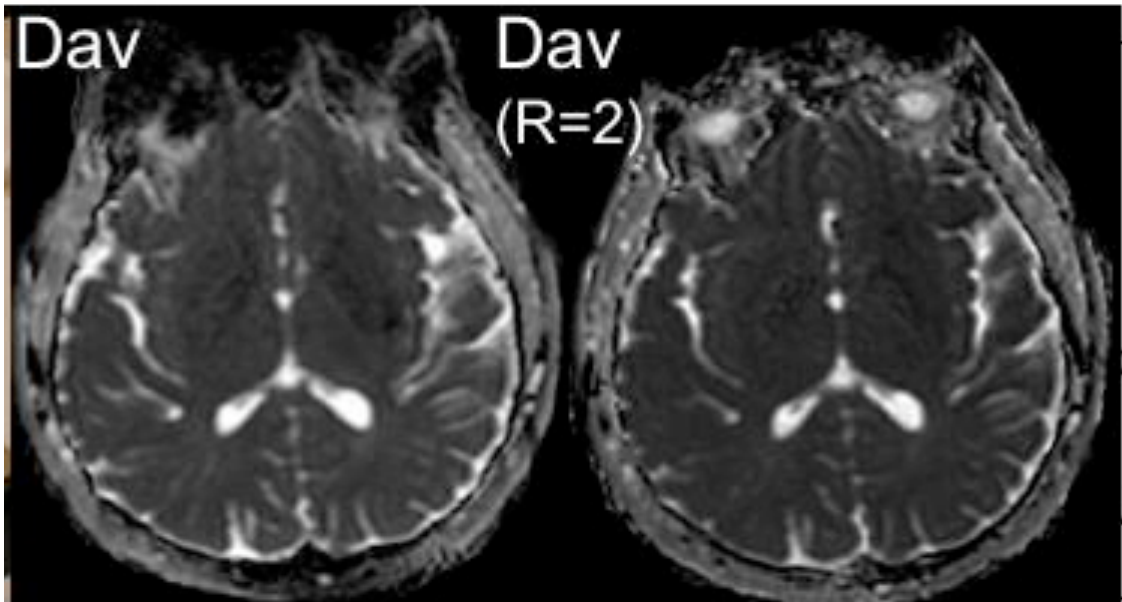


*Fig 4.1 – ssEPI diffusivity images acquired with (right) and without (left) SENSE (R=2)*

I also performed quantitative tests of the parallel imaging capability. I performed high angular resolution diffusion imaging (HARDI) with the coil using SENSE [33], and repeated the acquisition using a comparable commercial eight-channel head coil (55-direction axial single-shot EPI-SENSE with R=2 RL, 128x128, full-brain coverage, 2.2

mm isotropic resolution, TE = 100 ms, TR = 7 s, interleaved,  $N_{\text{ex}} = 3$ , b value = 1000 s/mm<sup>2</sup>, time = 15 min). The commercial coil has a radius of approximately 9.5 cm and length of 20 cm. To facilitate SNR comparisons between the coils, a neuroradiologist manually drew regions of interest containing a few key anatomical structures in the b=0 images. The SNR values in these structures in both sets of images were calculated, using a repeated scan technique that accounted for the non-uniform distribution of noise in the SENSE images [52].

In the EPI-SENSE HARDI data, the SNR in several important structures was markedly increased over the corresponding data collected with the commercial coil. For example, the SNR in the temporal stem and the forceps minor rose 56% and 48%, respectively. Due to the parallel encoding, the images were largely free from geometric distortions, signal dropouts, and blurring. The low-distortion SENSE performance agreed with our numerical simulations of the SENSE reconstruction. We computed the average g-factor over the sample to be very low at 1.01, reaching a peak value of 1.17.

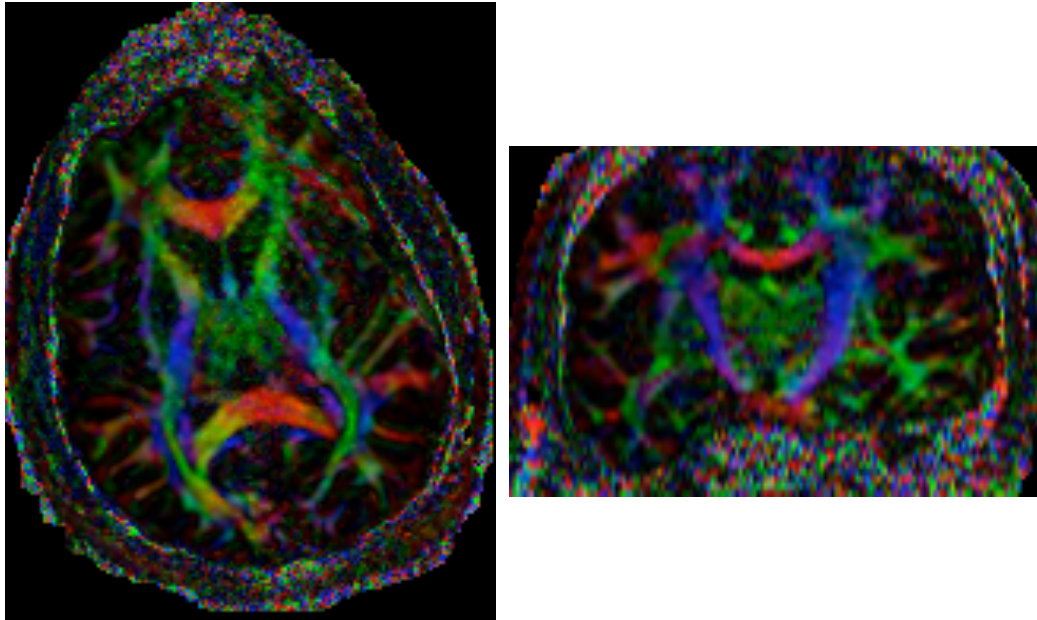


*Figure 4.2 Axial (left) and coronal (right) color-coded anisotropy maps, demonstrating the capability of the EPI-SENSE HARDI acquisition to identify detailed fiber tract anatomy. (Red = RL, Green = AP, Blue = SI)*

Parallel imaging is critical for high-field diffusion weighted imaging of the head, and the improved SNR of our coil over the commercial head coil in specific anatomic structures of interest demonstrates the advantage of our design in addressing an important clinical application.

## **4.3 Magnetic resonance spectroscopic imaging (MRSI) of the brain**

### **4.3.1 MRSI background**

MRSI allows non-invasive, localized measurement of the concentration of specific molecules (other than water) within tissues, providing a unique window into *in vivo* cell metabolism. MRSI relies on ppm differences in the main magnetic field experienced by protons in different molecules due to different electronic shielding, resulting in ppm changes in their Larmor frequencies, an effect known as the chemical shift

$$\delta = (\omega - \omega_{ref}) / \omega_{ref} .$$

A limited number of brain metabolites are measurable at clinical field strengths, including choline, creatine, N-acetyl aspartate (NAA), and lactate. Choline compounds (3.2ppm) are related to cell growth and cell membrane metabolism, exemplified by high levels in cancer patients and neonates [53]. Creatine compounds (mostly at 3.02ppm) are important in cellular energetics [54]. NAA (2.02ppm) is an important indicator for the status of neurons, and levels are known to be dramatically reduced in cancer (also low in neonates due to immaturity) [55]. Presence of lactate (1.33ppm) indicates anerobic metabolism, which can indicate growth that exceeds oxygen supply (e.g. cancer / neonate), mitochondrial dysfunction, or trauma [56]. Lipids, which are not normally found inside the brain but can wrap in from the skull, overlap lactate and complicate lactate measurement [55].

### **4.3.2 MRSI human studies**

To assess the performance of the coil for *in vivo* MRSI, I performed high resolution 3D MR spectroscopic imaging (MRSI) of the brain (0.22 cc, 8x8x8 PRESS, TE=35 ms, TR=1 s, time=8.5 minutes) on five normal volunteers on a GE 3 T MRI scanner using phased-array MRSI techniques [32].

In the 0.22 cm<sup>3</sup> spectroscopy data, a maximum SNR of 20.7 for the NAA peak in the cortical gray matter was achieved (fig. 5). The average value of the maximum SNR attained by the NAA peak in each exam was  $18.6 \pm 1.3$ .

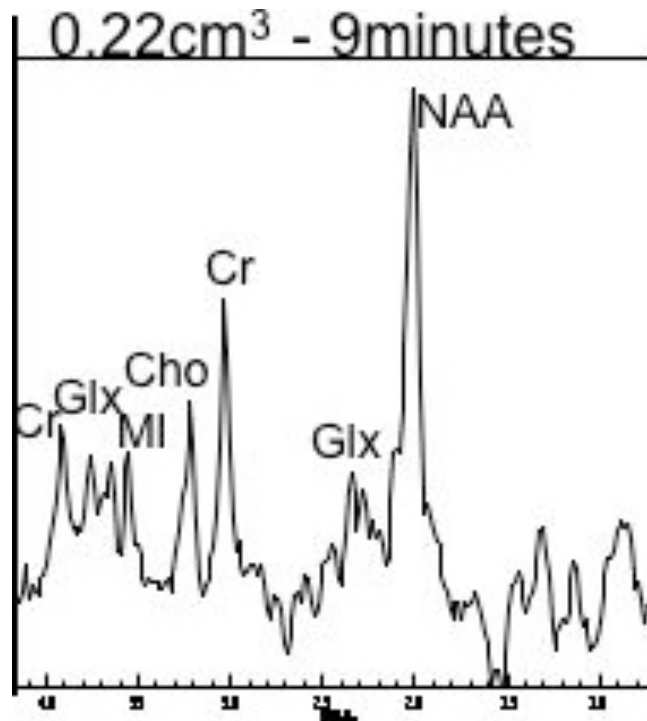


Figure 4.3 Spectra with SNR of 20.7 for NAA peak.

## **4.4 High resolution autocalibrating parallel MRI of trabecular bone in the hip**

### **4.4.1 High resolution MRI of trabecular bone**

Bone of the spine and articulating joints has an inner region of trabecular bone, consisting of a matrix of bony rods, filled with fatty bone marrow. The trabecular microarchitecture of bone undergoes degenerative changes in osteoporosis, resulting in destabilization and fracture [57]. The dimension of trabeculae is on the order of 100  $\mu\text{m}$ , pushing the practical spatial resolution and SNR limits of modern MRI scanners. High resolution MRI has emerged as a promising non-invasive technique for assessing the status of the trabecular microarchitecture [58, 59]. The combination of high field strength at 3.0T and a recently developed balanced steady-state free precession (b-SSFP) sequence maximizes the capabilities of this technique by providing high SNR at high spatial resolution [60]. The application of autocalibrating parallel encoding to this technique offers multiple advantages, including the flexibility to acquire more slices within a given acquisition time, and artifact reduction [61].

### **4.4.2 b-SSFP with parallel imaging**

In contrast to the spoiled gradient echo (SPGR) sequence described later for application to angiographic studies, SSFP sequences utilize phase coherent RF excitations (with  $0^\circ$  or  $180^\circ$  phase), with constant gradient-induced phase in each TR, which does not spoil the transverse magnetization by the end of each TR interval. In fully balanced sequences (b-SSFP or FIESTA), there is no net gradient area on any axis. A steady state transverse



magnetization is established, which has high signal and a complicated signal dependence, with approximately “T2 / T1” contrast weighting [26].

A key motivation for the application of parallel imaging to b-SSFP musculoskeletal studies is the ability to acquire more slices within a clinically reasonable scan time. More slices are useful for better image registration between studies. Parallel imaging can also be helpful for artifact suppression. Because of the strict condition on constant phase accrual in each TR interval, SSFP sequences are very sensitive to main magnetic field inhomogeneity, which inevitably arises in heterogeneous tissues such as bone due to varying magnetic susceptibility. Magnetic field inhomogeneity can cause banding artifacts with spacing inversely proportional to TR, which can ruin SSFP images [26]. A strategy for limiting banding is to collect two (or more) phase cycled scans (FIESTA-c). Using two phase cycles, acquisitions are done with and without sign alternation (or 180° phase) of the RF pulses. The locations of the bands are shifted in the two image sets, so taking the maximum value of the two acquisitions reduces the appearance of banding. Using parallel imaging, it is possible to collect more image sets with phase cycling within a given scan time, resulting in better artifact suppression. With more than two phase cycles, the image sets can be combined using a sum of squares of the image sets instead of a maximum value, utilizing more of the collected data and improving the SNR [61].

#### **4.4.3 Human hip studies**

In three normal volunteers coronal FIESTA-c images of the hip were acquired, using optimized sequence parameters [60] (FOV = 12 cm, 512 x 384, thickness = 1.5 mm, TR

= 8 s, TE = 2.32 ms, flip = 60, phase cycles = 2). These scans were carried out with full phase encoding, and subsequently with variable density GRAPPA undersampling at R = 2 - 4 along the RL direction. Acquisition times ranged from 11min10s (fully encoded) to 2min52s (4-fold acceleration). These images were reconstructed using a GRAPPA-based, customized offline reconstruction in Matlab [15, 62]. A similar repeated scan procedure was used for estimating the SNR in these images. All studies were conducted in compliance with the institutional review board, and informed consent was obtained.

In the GRAPPA images of the hip, the coil produced images of excellent quality using reduction factors as high as 4 (fig. 6). Prohibitively large extra SNR losses (beyond scan time) were not suffered. Parallel SNR was decreased versus the fully encoded SNR by a factor of 1.1-1.2 for R=2, 1.6-1.75 for R=3, and 2.1-2.4 for R=4.

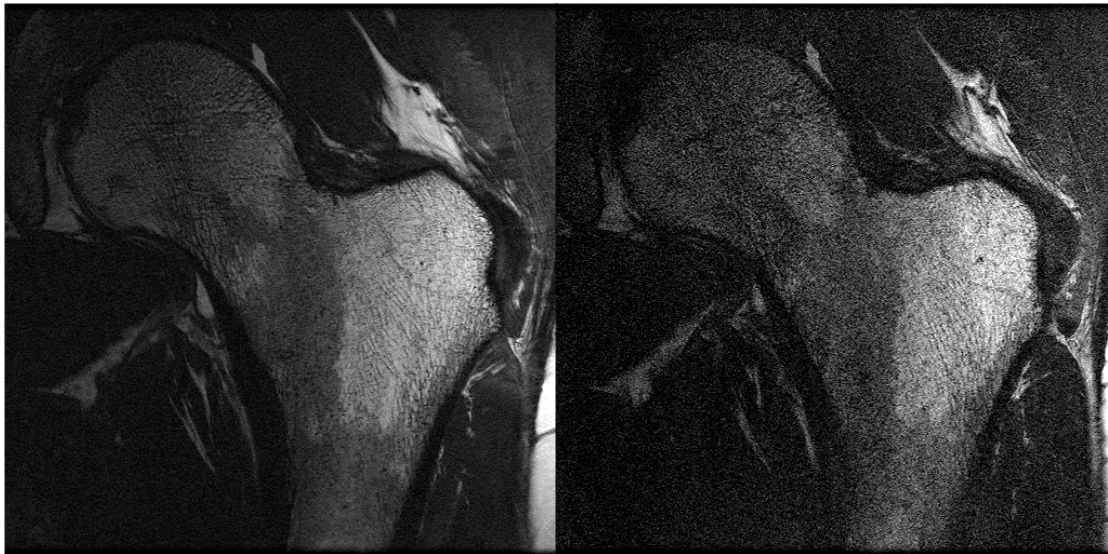


*Figure 4.4 Fully encoded coronal FIESTA image of hip (left) alongside rate-4 GRAPPA accelerated acquisition for the same slice (right). Both are sum of squares combined images.*

The good SNR obtained in the GRAPPA hip scans with up to a reduction factor of 4 introduces the possibility of reduced acquisition times, which is highly significant for the imaging of trabecular structure in osteoporosis or cartilage in osteoarthritis.

## **5 Intracranial Time-of-Flight (TOF) MRA at 7T using Phased Array Coils**

### **5.1 TOF Technique**

#### **5.1.1 TOF Background**

Time-of-flight (TOF) MRA is a safe, fully non-invasive cerebral angiographic technique with whole brain coverage at sub-millimeter spatial resolution, a combination of desirable properties that is unique among angiographic modalities. Catheter angiography still poses a small but significant risk of severe neurologic deficit [21] as well as other complications, such as arterial dissection [63]. This and CTA also carry risk of contrast-induced nephropathy [23], and administer substantial levels of ionizing radiation, which is causing increasing concern as a public health problem [25], especially in pediatric cases. Recently, gadolinium-based contrast agents have been linked to nephrogenic systemic fibrosis (NSF) in patients with pre-existing renal disease [28], which is particularly alarming for contrast enhanced (CE) MRA studies, which generally demand the highest dose of all CE procedures, sometimes double- or triple-dose [29]. Indeed, the first cases of NSF were identified in 1997, shortly after the introduction of gadolinium-enhanced MRA [27]. The toxicity of contrast agents is especially alarming when considering that the prevalence of end stage renal disease (ESRD) is expected to reach 785,000 by the year 2020, a 62% increase over 2005 numbers [30]. Therefore, high-resolution 3D TOF MRA within a clinically feasible acquisition time would be an attractive alternative for CTA or CE MRA, and a valuable screening procedure for diagnostic catheter angiography.

### **5.1.2 TOF Contrast**

The main source of vessel contrast in TOF MRA is inflow of fresh blood magnetization into the imaging slice or slab, which produces bright signal in regions with inflowing blood. This is in contrast to black blood imaging sequences, which are typically spin echo based, since the  $180^\circ$  pulse does not refocus blood that flows out of the imaging plane. TOF MRA is usually implemented as a spoiled gradient echo (SPGR) acquisition. In a spoiled GRE sequence, the transverse magnetization produced in a given RF excitation step does not persist beyond the end of that single TR interval [26]. Natural GRE spoiling can be accomplished by using a long TR  $\gg$  T<sub>2</sub>, but in SPGR spoiling is accomplished by varying the phases of the individual RF excitations, resulting in cancellations of residual transverse signals. Imaging with a relatively short TR (~ 10 - 50ms) results in signal saturation for stationary background tissues, and flow related enhancement (FRE) in regions where fresh blood flows into the imaging region and replenishes the longitudinal magnetization.

### **5.1.3 TOF artifacts and flow compensation**

The most important TOF artifact is signal saturation due to slowly flowing blood. Resulting “flow voids” are commonly seen clinically in stenosed vessels, for example. Other important TOF artifacts are due to flow of blood during and between the stages of MRI signal encoding and measurement, and can be minimized by minimizing the TE.

Two important TE-dependent artifacts are intravoxel dephasing and pulsatile flow artifacts. First, a spread of inflow velocities in a voxel (such as for laminar flow in a

small vessel) results in intravoxel dephasing and signal dropout if the TE is long enough. Second, blood flow rate is highly variable over the cardiac cycle, and in the intracranial vessels it is highly pulsatile, with most of the inflow concentrated over a short region of time following the R wave. This results in time-periodic view-to-view variations in the magnitude and phase of signals collected from vessel regions in subsequent phase encoding steps, which manifests as ringing artifacts along the phase encoding direction if the TE is long enough [64].

To minimize the TE, 3DTOF acquisitions use minimum phase RF pulse excitations with partial echo readout (with homodyne or conjugate symmetric reconstruction of the missing points) in order to minimize the TE. Sometimes the TE is set such that fat and water are out of phase, but this is not particularly important in intracranial TOF, so a minimum TE is usually chosen. Also, a slight compromise in TE may be made for flow compensation, which is a redesign of the sequence's gradient pulses to null first and/or higher order gradient moments and limit the two TE-dependent artifacts described above [26].

#### **5.1.4 Simulations for TOF contrast optimization**

I developed an FRE signal model to help determine the optimal acquisition parameters for TOF MRA. The spoiled GRE signal equation is [4]

$$S = M_0 \sin \theta \frac{1 - E_1}{1 - E_1 \cos \theta} E_2, \text{ where } E_1 = e^{-TR/T_1} \text{ and } E_2 = e^{-TR/T_2} \quad (5.1)$$

Inflow of blood into the imaging region can be modeled as an “effective T1” shortening, since T1 measures the rate of replenishment of longitudinal magnetization. This can be expressed as

$$\frac{1}{T_{1,eff}} = \frac{1}{T_{1,blood}} + \frac{1}{T_{1,flow}} = \frac{1}{T_{1,blood}} + \frac{v}{TH} \quad (5.2)$$

where  $v$  is the blood inflow velocity and  $TH$  is the slab or slice thickness [4]. A range of typical intracranial inflow velocities (5 – 50 cm/s) was considered, over a range of practical TR’s (1ms – 50ms) and flip angles (0 - 90°). A reasonable slab thickness of 2.4cm was used in this study. Contrast was determined by subtracting the background tissue signal from the blood signal. T1 relaxation times for blood and background tissue (gray matter) were taken from experimental 3T values in the literature, 1260ms and 1330ms, respectively [65, 66].

The results of the simulations I performed showed that the standard institutional clinical TOF MRA protocol (TR=20ms, flip=15°, TH=2.4cm) might be sub-optimal. An example contrast plot (for  $v=0.5\text{m/s}$ ) is shown in Figure 5.1. The contrast model predicted a benefit of imaging at very high flip angles, which is not practical, since slow and lateral flow is excessively saturated. However, a slightly higher repetition time and flip angle would be expected to improve the result substantially, as there is a steep edge of the contrast plot for short TR’s and small flip angles. Since the predicted improvement requires a longer acquisition time due to the longer TR, this analysis also raises the question of an optimally time-efficient sequence, since total acquisition time is a free parameter thanks to parallel imaging. This question is addressed in the human studies to

be presented later, through quantitative comparison between different acquisition parameters.

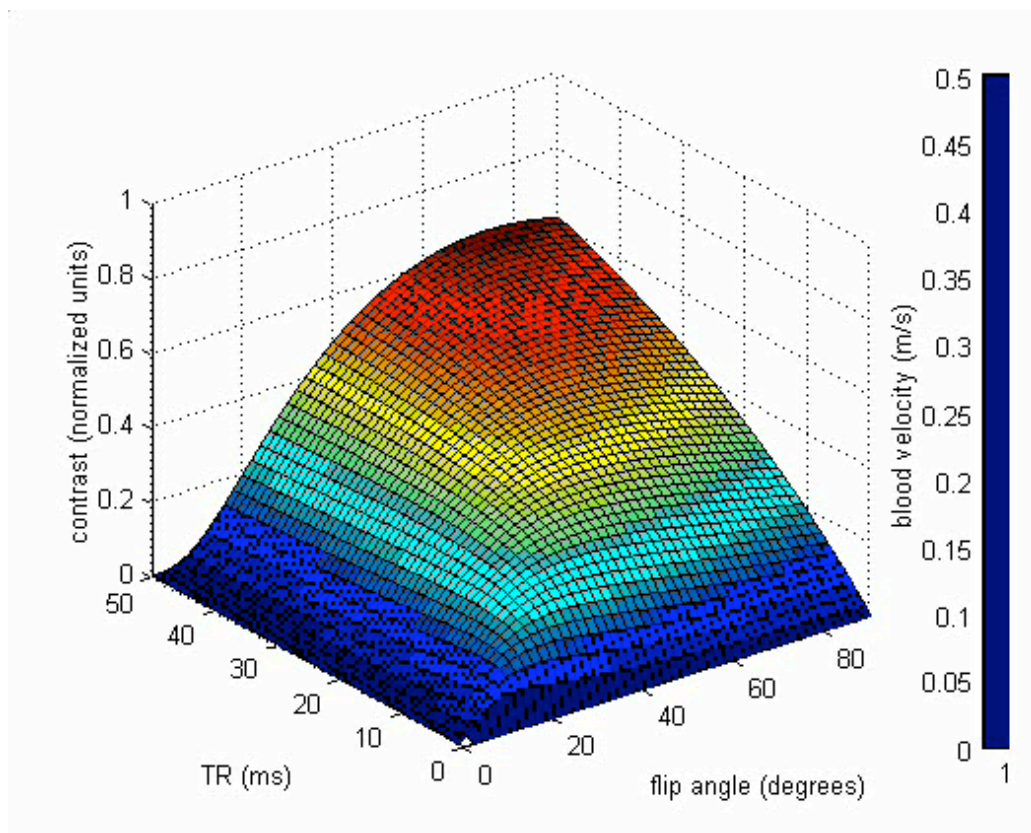


*Figure 5.1 Surface contrast plot showing dependence of vessel contrast on TR and flip angle, for a given blood inflow velocity of 0.5m/s*

### **5.1.5 Multiple overlapping thin slab acquisition (MOTSA) technique**

The MOTSA technique [67] is the most popular implementation of TOF MRA. In this technique, the imaging volume is divided into multiple 3D slabs. This reduces the dramatic saturation of blood that occurs due to exposure to multiple RF pulses before exiting the top of a single larger slab. Vessels near the leading edge of the slab are brighter than others, so this is sometimes known as the entry slice effect. In MOTSA, the



reduced SNR due to excitation of a smaller volume must be balanced against the reduction of the “Venetian blind” artifact associated with larger individual slabs, due to the entry slice effect. In TOF MRA of regions of the body with slower inflow (e.g. MRA of the extremities), this approach is carried to its limit in 2D TOF MRA. 2D TOF is also useful for venography of the brain, when combined with sub-slab saturation pulses to eliminate arterial signal. In MOTSA, adjacent slabs are overlapped by a few slices, again to reduce the appearance of saturation artifacts.

### **5.1.6 Clinical applications of TOF MRA**

Since it can be easily tacked on to any set of MRI studies, TOF MRA is an easy and useful study for many vascular diseases. In particular, TOF MRA at 3T is the current MRI method of choice for the clinical evaluation of intracranial aneurysms [68, 69], the leading cause of non-traumatic subarachnoid hemorrhage (SAH) [70]. The annual US incidence of SAH is approximately 21,000-33,000, with fatality rate estimates ranging from 32-63%, and 10-20% of patients experiencing moderate to severe disability on discharge from the hospital [71].

## ***5.2 TOF MRA human studies at 7T with comparison to 3T***

### **5.2.1 Overview**

Higher field strengths are particularly beneficial to time-of-flight (TOF) MRA techniques. Compared to lower field strengths vessel contrast is increased both by the higher SNR and by the greater background suppression afforded by longer T1 relaxation

times of static background tissue. Increased contrast and spatial resolution are highly desirable for more sensitive detection of small aneurysms and vasculitis and for improved morphological characterization of larger aneurysms. On these bases, intracranial TOF image quality improvements have previously been described in the transition from 1.5T to 3T [65, 69, 72], and 3T to 4.7T [73]. The quantitative performance of TOF MRA at 7T had, to my knowledge, not previously been investigated. Recently a preliminary study showed intracranial TOF images at 7T [74], but no quantitative comparison between field strengths or acquisition parameters was presented. Also, only volume RF receiver coils were used, which have inferior SNR performance versus phased array coils, especially at higher field strengths [75]. The goal of this study [76] was to investigate the feasibility of 7T intracranial TOF MRA using phased array coils and assess performance at 7T as compared to 3T in normal volunteer studies using identical parameters at the two field strengths and using scanners from the same manufacturer with the same software version.

In an initial study, I scanned five normal volunteers at 3T and 7T using standard acquisition parameters from a clinical TOF protocol. Contrast-to-noise (CNR) values were measured for selected major vessel segments, documenting a mean CNR increase of 83%. In a second study, I scanned three normal volunteers at 3T and 7T using empirically optimized 7T parameters. The CNR values achieved using the latter protocol were similar to the values obtained in the initial study, despite the 42% reduction expected due to the higher spatial resolution. CNR in the smaller peripheral vessels was increased dramatically, resulting in excellent visualization at high resolution. In summary, TOF MRA at 7T demonstrated improved visualization of the intracranial vasculature,

particularly the smaller peripheral vessels, and may benefit studies of small aneurysms, atherosclerosis, vasospasm, and vasculitis.

## **5.2.2 Methods**

### *MRI Hardware*

All MR data was acquired on a 3T GE Signa EXCITE system, and a prototype 7T GE system (GE Healthcare, Waukesha, WI). Standard body coil transmit was employed at 3T, while a transmitter insert coil was used at 7T (Nova Medical, Wilmington, MA). Eight-channel phased array receive coils were used at both field strengths, although the 7T head coil consists of smaller, non-overlapping elements [77], in contrast to the manufacturer-supplied 3T head coil.

### *Human Subjects*

Five normal adult volunteers were scanned at both field strengths for the initial study, and three normal adult volunteers were scanned in the second study. All studies were conducted in accordance with the regulations of the Committee on Human Research at our institution, and written informed consent was obtained from each subject.

### *Acquisition protocol*

Identical acquisition parameters were used at both field strengths, according to a standard clinical protocol for intracranial TOF MRA at our institution (matrix 384x224x120, FOV=24cm x 16cm x 12cm, TR=20ms, TE=2.5ms, flip=15°, readout bandwidth=32kHz). The nominal spatial resolution was 0.63mm (frequency, anterior-

posterior) x 0.80mm (phase, right-left) x 1 mm (slice, superior-inferior). The acquisition was divided into five slabs, employing the MOTSA (multiple overlapping thin slab acquisition) technique [67]. MRA was graphically prescribed on standard three-plane localizers. The slabs were positioned axially, parallel to the intercommissural line, and spanned levels extending from the petrous internal carotids to the vertex. Each slab consisted of 24 1.0-mm thick partitions (including 6 overlapping slices per slab). This resulted in a total scan time of 7min, 1sec. To minimize artifacts and signal loss due to blood flow, a minimum phase RF pulse with fractional echo readout enabled the short echo time. First order flow compensation was applied to the slab and readout gradient waveforms, at the cost of a slight increase in TE (from 1.9ms to 2.5ms). Due to FDA limitations on specific absorption rate (SAR) encountered at 7T, no venous spatial saturation or magnetization transfer pulses were used.

Following this initial comparison between field strengths, a second series of experiments was performed in order to improve the acquisition protocol and thus more fully explore the capabilities of TOF MRA at 7T. Specifically, the TR, flip angle, slice and slab thickness were varied empirically at 7T, while maintaining the position of the leading edge of the graphic prescription in order to keep inflow effects constant. The parameter space was searched for the best combination of contrast and resolution in one or two slabs. Three additional volunteers were scanned with full coverage at 3T and 7T using the resultant improved protocol (TR=30ms, flip=25°, each slab = 38 slices x 0.5mm thick). Reduction in the superior coverage (using four of the smaller slabs instead of five larger slabs) was accepted in order to limit the scan time to 13min, 1sec.

### *Analysis Methods*

To quantify the results, CNR measurements for major arterial segments were obtained directly from the source images. I drew ROI's manually on each scan, within the anterior (M1, A2) and posterior (P1/P2) circulation, as well as superior portions of the internal carotids and basilar arteries. Regions of background brain tissue and noise outside the head were also selected. For each scan, I calculated CNR by subtracting the average intensity value of the background tissue from the average value of each arterial segment, and dividing by the average of the noise regions. Since magnitude images were used, the standard scaling factor of 0.8 was applied to each noise number [78], although this does not affect any fractional changes observed.

### **5.2.3 Results**

TOF angiography at 7T resulted in improved vessel contrast throughout the intracranial vasculature in all five volunteers in the initial study. Sample pairs of comparison images are shown in Figure 5.2. Reduced contrast in the background tissues is evident in the 7T images, indicating improved background suppression. The projections also show improved visibility of the posterior communicating arteries at 7T.

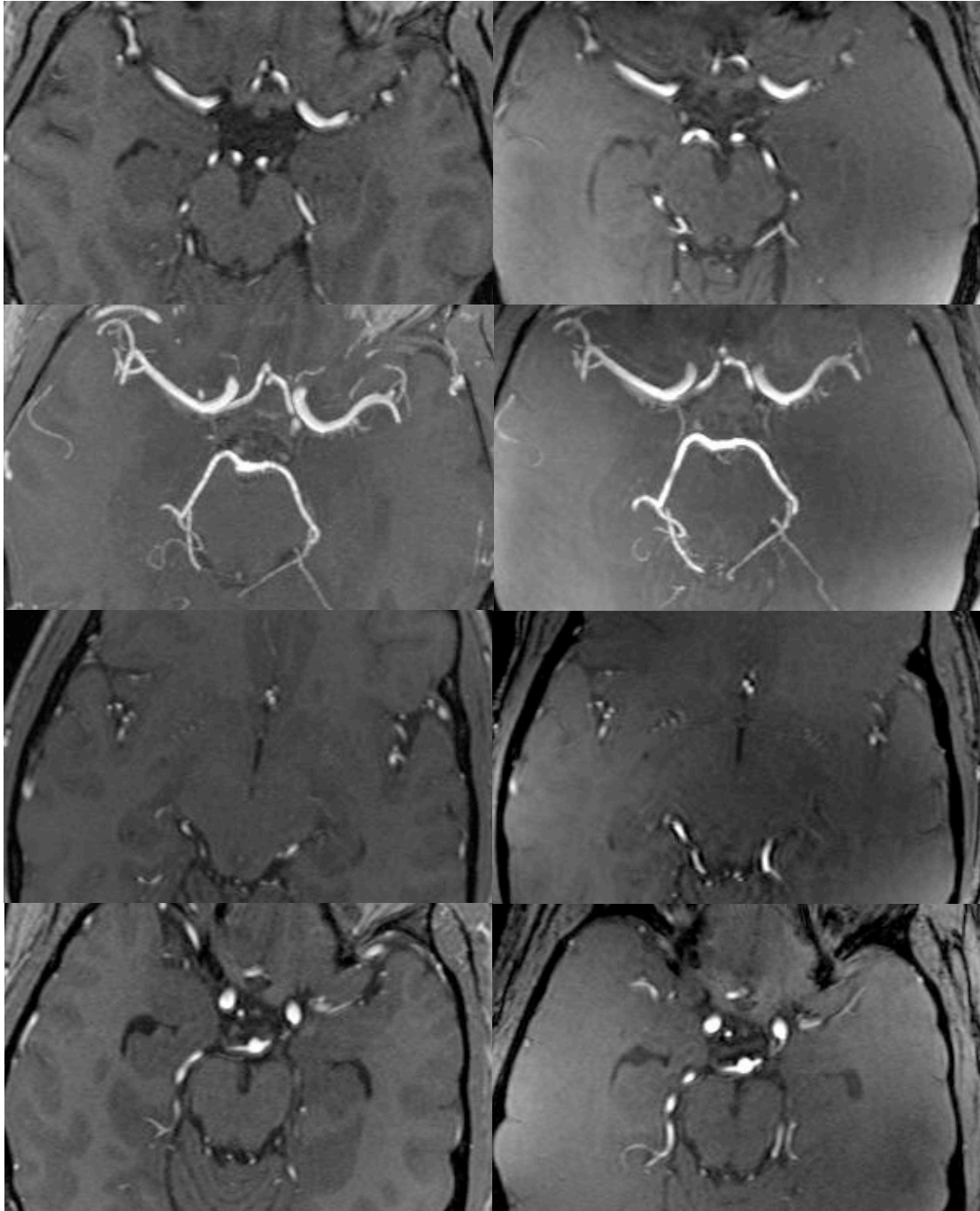


*Figure 5.2 Comparison of 3T and 7T images in a normal volunteer. Top row: A pair of source images (left- 3T, right- 7T) showing portions of M1 and P1/P2 segments. 2<sup>nd</sup> row: MIP of a 7mm slab, 3<sup>rd</sup> row: A2's, 4<sup>th</sup> row: ICA's, basilar artery*

All individual vascular CNR comparisons showed improvements at 7T over 3T, ranging from 33% - 134%. The average CNR increase among all individual measurements was 83%, with a median increase of 77%. Some results of the CNR measurements are presented in Figure 5.3.

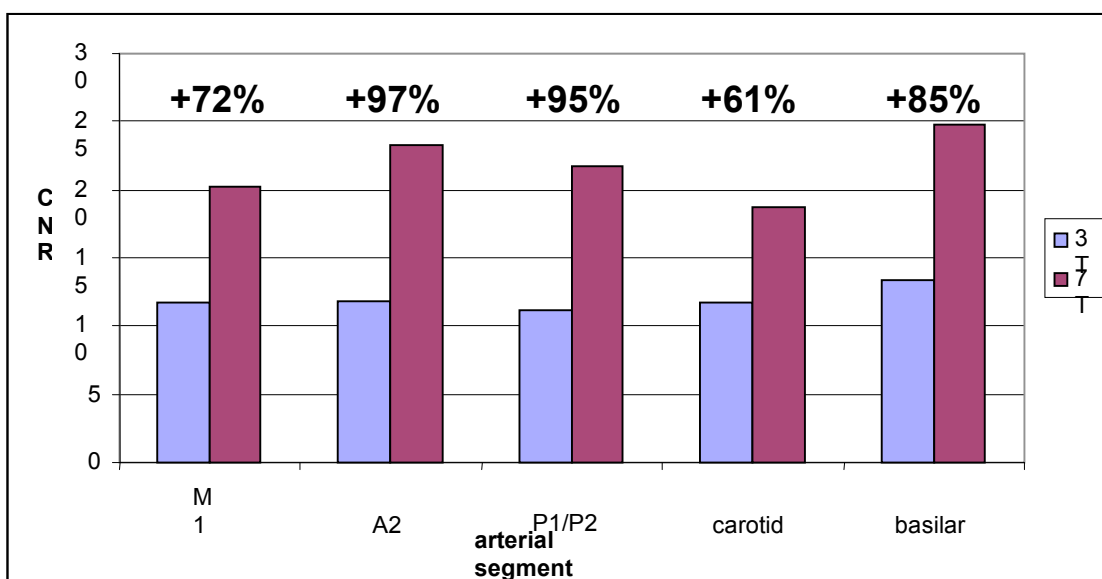
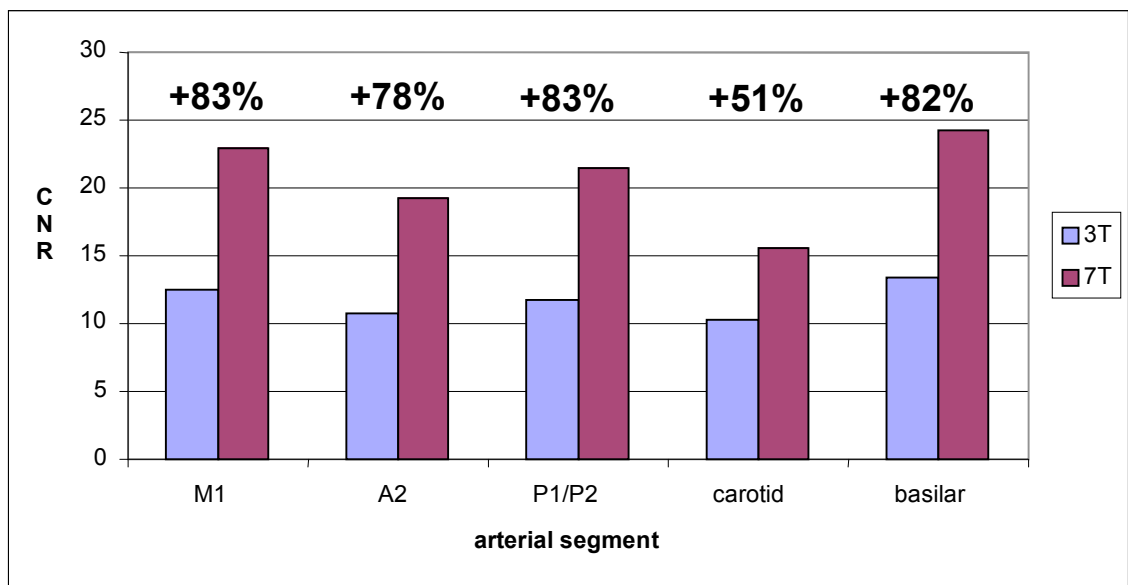


Figure 5.3 Mean CNR for 3T and 7T acquisitions, grouped by arterial segment

Based on this preliminary study, I determined that the increased CNR at 7T would allow doubling the spatial resolution to 0.5-mm slice thickness. The number of slice encodes was increased from 24 to 38 in order to maintain a similar slab thickness. Also, varying the TR / flip angle combination showed that a somewhat longer TR and larger flip (30ms / 25°) improved the contrast throughout the vasculature at both 7T and 3T, in agreement with the FRE simulations I had conducted.

For the major segments studied above, the CNR values achieved using the improved protocol were comparable to values obtained in the initial study, despite the expected 42% CNR loss due to the halved voxel size (after accounting for the increased number of signal averages). These CNR numbers are given in Figure 5.4. Also, the CNR increases between 3T and 7T for the 0.5mm slice data were comparable to the increases seen in the 1mm data.



*Figure 5.4 Average CNR values obtained using improved acquisition parameters*

CNR in the smaller peripheral blood vessels was increased dramatically in the 7T images, especially in the higher resolution studies. The maximum intensity projections through the 0.5mm slice data in Figure 5.5 demonstrate the superior arterial contrast at 7T. Contrast improvements are especially apparent in the peripheral branches of the MCA's.



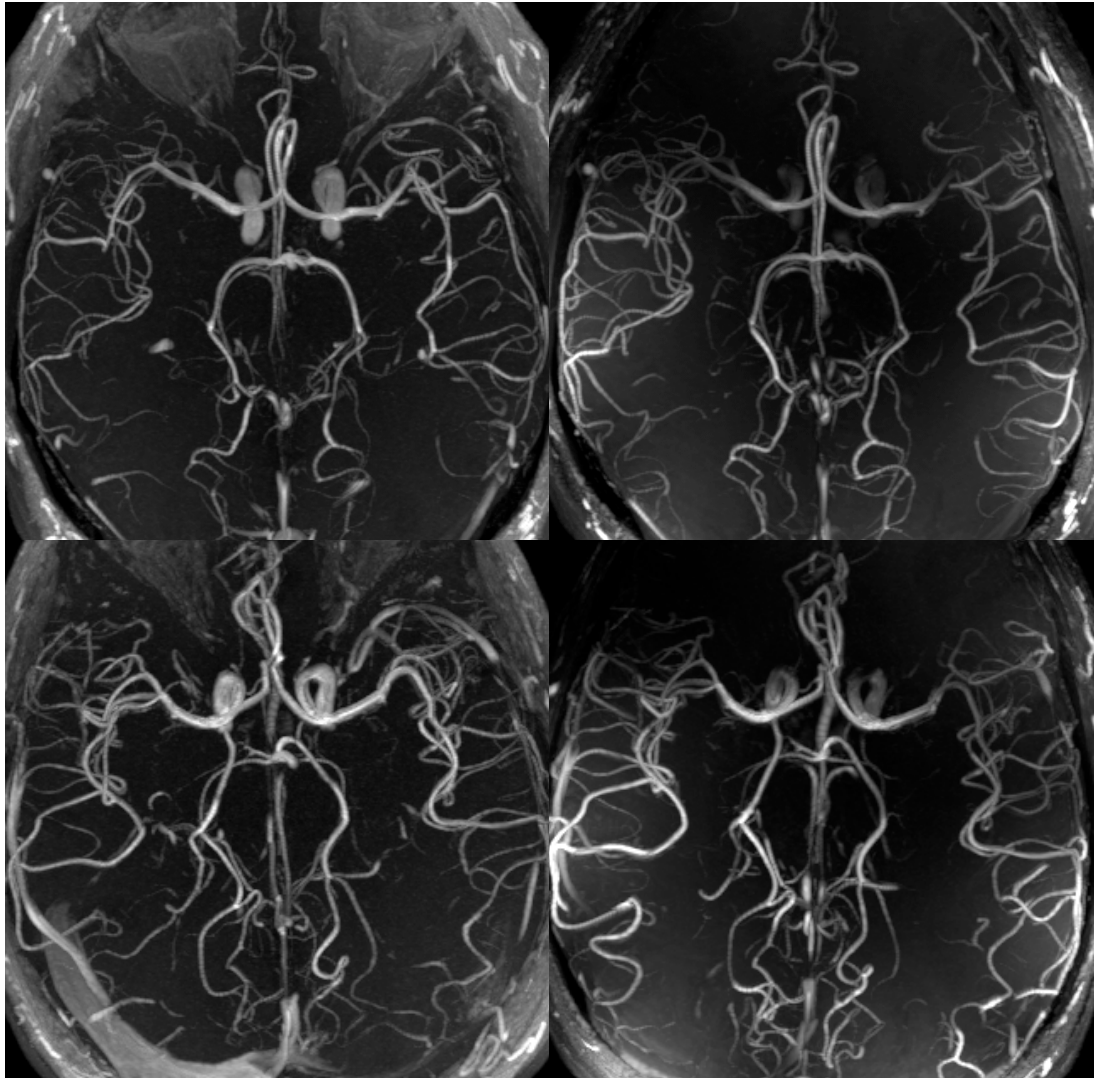


*Figure 5.5 Axial MIP's from two normal adult volunteers at both field strengths (left – 3T, right – 7T)*

Sagittal maximum intensity projection through the right half of the intracranial vasculature after cropping the edges of the head using a Vitrea workstation (Vital Images, Inc., Minnetonka, MN) shows the superior-inferior extent of vessels more clearly (Figure 5.6). This targeted MIP reconstruction also demonstrates low venous contamination, as exemplified by the minimal conspicuity of the superior sagittal sinus, even without any venous spatial saturation pulses, and using a set of acquisition parameters sensitized to slow flow.

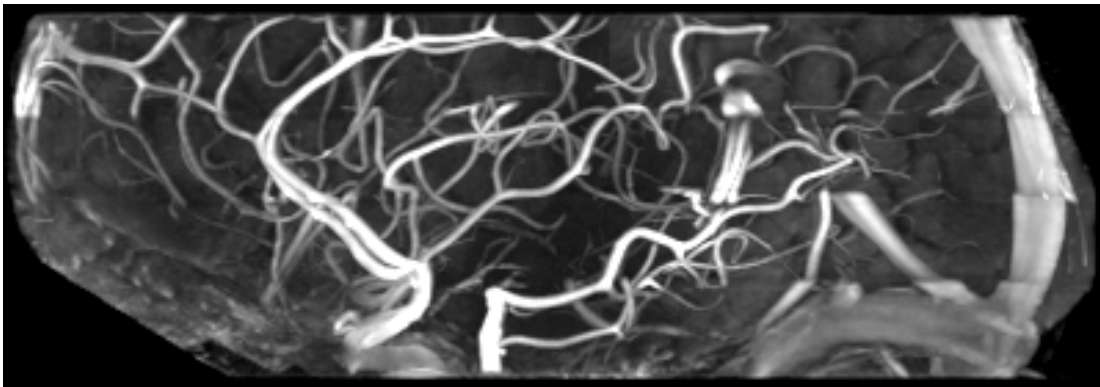


*Figure 5.6 Sagittal MIP through the right half of 7T MRA data with removal of superficial calvarium and scalp soft tissues*

#### **5.2.4 Discussion**

This initial 7T MRA study documented large improvements in vessel contrast at 7T in comparison to 3T. In theory, the CNR should increase by a factor of about  $7 / 3$  due to the linear increase of SNR [79], and by an additional factor due to the longer T1 of the background tissue [69, 72]. Nevertheless, combining all individual comparisons among both studies, the actual average increase of 81% is somewhat less than the probable

predicted increase. There are several possible explanations for the lower than anticipated CNR increases. First of all, the smallest individual CNR increases (30%, 33%, 38%) occurred in the most inferior vessels (basilar and internal carotids), where there was a falloff in coil sensitivity at 7T due to the smaller coil geometry. At these caudal levels of acquisition in the region of the air-filled paranasal sinuses and petrous apices, the greater impact of magnetic susceptibility at 7T also reduced the signal in some cases. Second, as with background brain parenchyma, the T1 of the blood pool is longer at higher field and saturates with short TR sequences. Comparing 1.5T to 3T, the fractional T1 increases were larger for background tissues than for blood [72], and it is not known whether this trend continues to 7T. Third, significant reductions in measured CNR probably arise due to the partial voluming of blood in voxels at vessel edges, if these regions are included in the analysis. And finally, further uncertainties are introduced because of the impossibility of duplicating graphic prescriptions between scanners, and tracing exactly the same ROIs on the source images.

Pulsatile blood flow through the more inhomogeneous B0 field at 7T could result in worsened ghosting and signal loss [64], but this effect did not appear to be particularly significant, probably because the echo time used was sufficiently short. Some increased ghosting along the phase encoding directions was seen around faster-flowing vessels in some of the 7T images, but this could be attributable to ordinary flow pulsatility effects magnified by the higher signal-to-noise (and thus artifact-to-noise) at 7T. More significant was the increased frequency encoding ringing observed in the vicinity of the

MCA in a few of the data sets (e.g. Figure 5.2), which might be alleviated by increasing the matrix size.

The most significant finding in our study was the excellent visualization of smaller peripheral vessels at 7T. This is due to the combination of the higher field strength, longer background T1, the unique phased array coil (consisting of smaller elements with higher peripheral sensitivity), and the improved acquisition parameters.

The contrast improvements seen with the improved sequence are probably the net result of several influences. First, the longer TR / larger flip angle combination results in reduced saturation of slower flowing blood versus static background tissue. Second, there is different T1 contrast between blood and background signal. Since the actual T1 values are unknown, it is not known whether the parameter changes were beneficial or detrimental in this regard at 7T, although the improved contrast clearly indicates the superiority of the new parameters. Third, it is important to note that increasing the resolution does not necessarily reduce contrast in vessels of sub-voxel dimensions because there is less partial voluming, and contrast may actually be improved when intravoxel dephasing is reduced.

The drawback of both the longer TR and higher resolution is the extended acquisition time. The longer TR increases the scan time by 50%, and doubling the resolution increases it another 100%. However, the new TR and flip angle are certainly more efficient. Since the overall CNR was about the same for both sets of acquisition

parameters despite a 42% expected CNR reduction due to resolution and signal averaging changes (based on CNR measurements in the larger vessels where the aforementioned resolution effects are absent), it can be reasoned that the new TR / flip angle combination improves contrast by approximately 72%. This CNR increase outweighs the scan time increase, due to the possibility for parallel imaging. Estimating the CNR losses due to a hypothetical rate-1.5 parallel imaging scan using the longer TR / higher flip angle parameters (thus equalizing the scan time, resolution and coverage with the shorter TR / lower flip angle unaccelerated scan), the accelerated scan would still produce about 42% more CNR than the unaccelerated version, ignoring reconstruction related losses (i.e. the g-factor in SENSE [16]). CNR improvements would be seen at g-factors up to 1.42, which is much larger than would be expected anywhere in the imaging volume at this reduction factor, especially for a receiver array specifically designed for parallel imaging [35].

### **5.2.5 Conclusion**

This study demonstrated the high quality of phased-array 7T intracranial TOF MRA with significant improvements in vessel contrast over 3T. At 7T, I showed TOF to be sensitive to the slowly flowing blood of smaller peripheral vessels when appropriate acquisition parameters are used. I expect this technique to be useful for studying small aneurysms, atherosclerosis, vasospasm, and possibly vasculitis.

The measurable improvement in imaging performance when going to higher spatial resolution at 7T raises the question of whether pushing the resolution even further will yield even more benefits. However, the exploration of this question will require that the barrier of prohibitive scan times associated with high resolution protocols must be overcome.

## **6 Accelerated autocalibrating high resolution TOF MRA at 7T**

### **6.1 Overview**

High resolution 3D TOF MRA within a clinically feasible acquisition time would be an attractive alternative for CTA or CE MRA, and a valuable screening procedure for diagnostic catheter angiography. Higher resolution intracranial 3D TOF MRA studies are desirable for detecting subtle pathology of the intracranial circulation. This is especially true in the case of atherosclerosis of distal arterial branches, cerebral vasculitis, and small intracranial aneurysms. Increased SNR and better background suppression (due to the longer T1 relaxation times of background brain tissues) at high field yield enhanced vessel CNR, and thus enable higher spatial resolution angiography [65, 72, 76]. However, at very high field strengths, the extended scan time needed for sequential phase encoding of the larger matrix is not clinically feasible. Parallel imaging techniques can accelerate scans at the expense of SNR, but SNR may be regained at higher resolutions if the effects of partial voluming and/or intravoxel dephasing are reduced. In this study, I developed a customized auto-calibrating parallel imaging technique and applied it to 7T TOF MRA, achieving very high resolution MRA studies of normal volunteers and patients with cerebrovascular disease within a reasonable scan time.

## 6.2 Generalized autocalibrating partially parallel acquisition (GRAPPA) imaging

### 6.2.1 GRAPPA overview

In SMASH (Sec 2.3.3), data from undersampled individual coil images is combined into a single composite image. GRAPPA [15] is an extension of SMASH that decouples image reconstruction from individual coil image combination. GRAPPA generates full images for each coil from undersampled data, allowing better coil image combination techniques (e.g. sum of squares) for improved SNR. Another advantage of GRAPPA is that it is autocalibrating, meaning that it does not require a separate sensitivity calibration scan.

### 6.2.2 GRAPPA reconstruction

In GRAPPA, undersampled individual coil images may be combined to form missing data from a single coil  $p$ , separated from acquired data by a known spatial harmonic  $e^{jm\Delta ky}$ , using the relationship (modified from Eq. 2.28)

$$\sum_{n=1}^{N_{coils}} a_{n,m} \int_x \int_y C_n(x,y) M(x,y) e^{-2\pi j [k_x(t)x + k_y(t)y]} dx dy = \int_x \int_y C_p(x,y) M(x,y) e^{-2\pi j [k_x(t)x + k_y(t)y]} e^{jm\Delta ky} dx dy \quad (6.1)$$

with all quantities as defined in Sec 2.3.3. Instead of separately fitting coil sensitivity maps as in SMASH, the combination coefficients ( $a$ 's) are determined by direct fitting among several adjacent lines in a training region of fully sampled  $k$ -space, known as the autocalibrating signal (ACS) block.



Outside the ACS block, phase encoding lines are undersampled by a factor of ORF (the outer reduction factor), which is analogous to the reduction factor R in SENSE and SMASH. The scanner pulse sequence must be modified to sample k-space with this variable density. For this reason, the scan time reduction is slightly less than a factor of ORF. Due to less signal averaging, the SNR of the GRAPPA acquisition is reduced by at least slightly less than  $\sqrt{ORF}$ .

For missing data  $S_j$  in a given  $j^{\text{th}}$  coil and corresponding to a particular spatial harmonic  $m$ , data from a number of adjacent lines (or GRAPPA blocks) are combined according to

$$S_j(k_y - m\Delta k_y) = \sum_{n=1}^{N_{\text{coils}}} \sum_{b=-N_b/2}^{N_b/2-1} a_{j,b,n,m} S_n(k_y - ORF\Delta k_y) \quad (6.2)$$

where  $b$  counts through the GRAPPA blocks and  $n$  counts through the individual coils.

By considering signal variation orthogonal to the acceleration direction, a GRAPPA reconstruction kernel with expanded dimensionality, such as the multi-column multi-line interpolation (MCMLI) GRAPPA-based technique proposed by Wang et al [80], can improve the quality of the data fitting. In this technique, additional fitting parameters are included in the GRAPPA kernel, corresponding to 2D spatial harmonics that are pairings of spatial harmonics orthogonal to the acceleration direction with the standard spatial harmonics in the acceleration direction. The signal synthesis procedure is described by

$$S_j(k_y + m\Delta k_y, k_x) = \sum_{n=1}^{N_{\text{coils}}} \sum_{b=-N_b/2}^{N_b/2-1} \sum_{h=-N_h/2}^{N_h/2-1} a_{j,b,n,m,h} S_n(k_y + bORF\Delta k_y, k_x + h\Delta k_x) \quad (6.3)$$

where  $h$  counts through the  $N_h$  orthogonal spatial harmonics. In cases where the terms based on 1D spatial harmonic functions fail to model signal variation in the image, such an approach may produce better results.

### **6.3 Methods**

#### *MRI Hardware-*

MRA was performed using a research 7T system (GE Healthcare, Waukesha, WI) with custom insert transmitter and eight-channel phased array receiver coils (Nova Medical, Wilmington, MA).

#### *Acquisition parameters-*

The TR (30ms), flip angle ( $25^\circ$ ), slab size, and slice thickness were taken from an initial 7T study [76], where these parameters were empirically optimized for the multiple overlapping thin slab acquisition (MOTSA) technique [67]. For each exam, four 1.9-cm slabs were acquired, each consisting of 38 x 0.5-mm slices, including six overlapping slices per slab. The in-plane matrix size was expanded to 512x384 from 384x224, over the same field-of-view of 22cm (phase FOV=0.75). The voxel size was thus reduced to  $0.146\text{mm}^3$  from  $0.335\text{mm}^3$ . The readout bandwidth was increased to  $\pm 62.5\text{kHz}$  from  $\pm 32\text{kHz}$  to achieve a similar TE (2.6ms, including flow compensation along slab and read directions) and bandwidth per pixel along the larger frequency encoding dimension (332 points vs. 248 points, using 65% fractional echo readout), in order to limit the susceptibility-induced signal dropouts observed previously in the internal carotids [76], as well as artifacts due to blood flow. A fully encoded scan would have required 22min, 7

sec. Instead, data was undersampled with variable density along the in-plane phase encoding direction, with outer reduction factor (ORF) = 2 around a central block sampled at Nyquist rate, containing 12 acquired auto-calibrating signal (ACS) lines [15]. The total scan time was thus reduced to 12min, 45s, which is slightly less than the prior 7T MRA study [76].

*Reconstruction details-*

Images were reconstructed first using standard GRAPPA reconstruction [15]. For missing data  $S_j$  in a given  $j^{\text{th}}$  coil and corresponding to a particular spatial harmonic  $m$ , acquired data from  $N_b$  adjacent lines (or GRAPPA blocks) were combined according to

$$S_j(k_y + m\Delta k_y) = \sum_{n=1}^{N_{\text{coils}}} \sum_{b=-N_b/2}^{N_b/2-1} a_{j,b,n,m} S_n(k_y + bORF\Delta k_y) \quad (6.4)$$

where  $b$  counts through the GRAPPA blocks and  $n$  counts through the  $N_{\text{coils}}$  individual coils. Six to twelve GRAPPA blocks were used to reconstruct the data, with kernel coefficients ( $a_{j,b,n,m}$ 's) determined by least squares fitting among several central acquired lines among all coils. The same raw data was subsequently reconstructed using an expanded GRAPPA-based reconstruction kernel including additional terms incorporating products of first-order spatial harmonics along the frequency encoding direction, thus employing a form of the multi-column multi-line interpolation (MCMLI) technique proposed by Wang et al[80]. In this case, the signal synthesis procedure is described by

$$S_j(k_y + m\Delta k_y, k_x) = \sum_{n=1}^{N_{\text{coils}}} \sum_{b=-N_b/2}^{N_b/2-1} \sum_{h=-N_h/2}^{N_h/2-1} a_{j,b,n,m,h} S_n(k_y + bORF\Delta k_y, k_x + h\Delta k_x) \quad (6.5)$$

where  $h$  counts through the  $N_h$  orthogonal harmonics (in this case, one). The reconstruction software was coded in Matlab (The MathWorks, Natick, MA). For display

purposes, data was zero-filled in all dimensions (to 1024x768x268), and the sum-of-squares images were filter corrected to remove the effect of surface coil sensitivity variation [81].

#### *Human studies-*

The described MRA protocol was applied to seven normal adult volunteers and three patients with known cerebrovascular disease. The disorders in the three patients were a history of internal carotid artery (ICA) dissection, stenosis of the middle cerebral artery (MCA), and an arteriovenous malformation (AVM), respectively. MRA slabs were prescribed on standard three-plane localizers and positioned axially, extending from the petrous internal carotids towards the vertex. All studies were conducted in accordance with the regulations of the Committee on Human Research at our institution, and written informed consent was obtained from each subject.

## **6.4 Results**

While the standard GRAPPA reconstruction was generally successful, it resulted in significant residual aliasing artifacts in certain imaged regions, whereas the expanded GRAPPA-based reconstruction reduced this to a negligible level throughout the imaging volume. A reconstruction kernel size of eight blocks gave the best results for both techniques. Figure 6.1 presents a side-by-side comparison of two typical reconstructions in axial targeted maximum intensity projections (MIP's) through the same imaging volume in one volunteer.

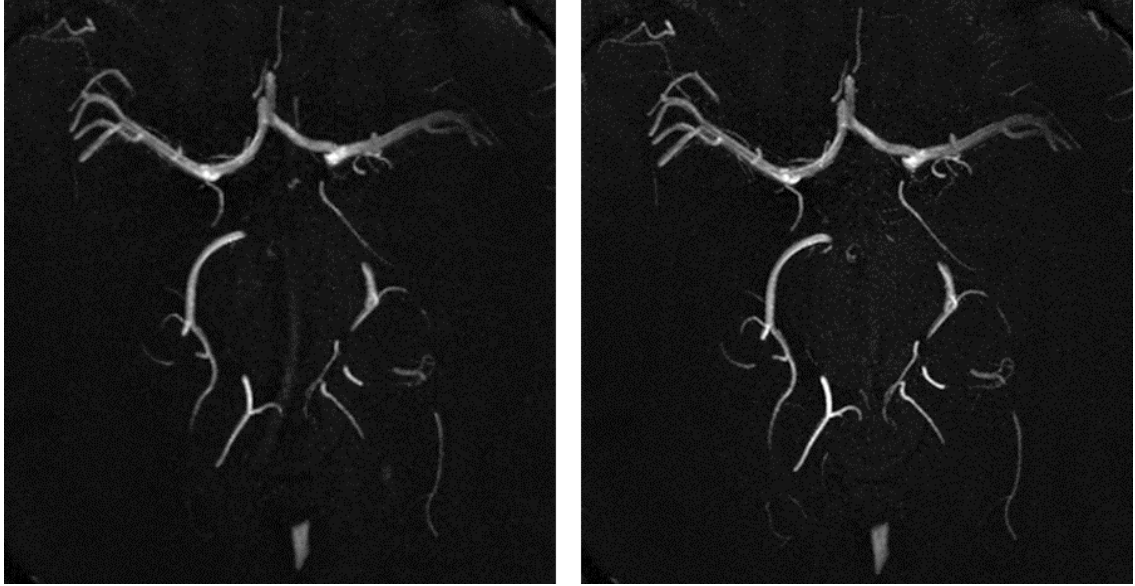


*Figure 6.1 - Axial MIPs (8mm) through the same imaging region, showing data reconstructed using standard GRAPPA (left), with increased artifact, and the customized autocalibrating reconstruction (right)*

The described protocol with the customized auto-calibrating reconstruction produced MR angiograms that were largely free from artifacts for all volunteers and patients. As expected because of the similar TE, artifacts due to pulsatile blood flow were limited and comparable to those in the initial study [76].

Results from the new protocol compared favorably to those previously obtained using a lower resolution protocol, with nearly equal scan time and coverage [76]. As seen in

Figure 6.2, the higher resolution protocol yields improved depiction of the small peripheral vessels in the brain.

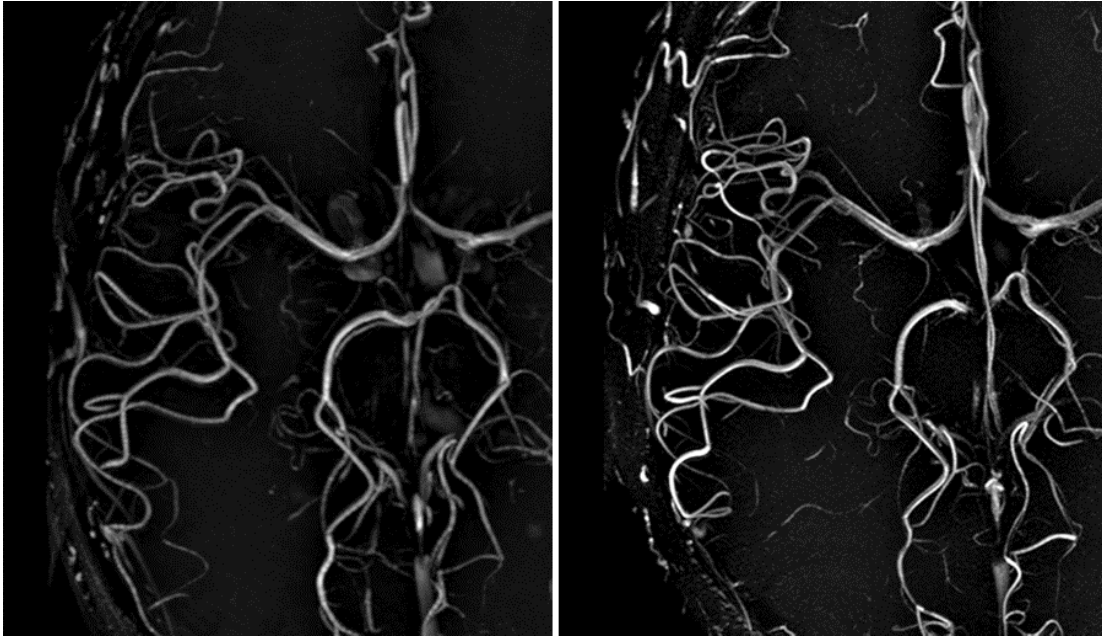


*Figure 6.2 – Full axial MIPs through MRA images from same volunteer using original, lower resolution protocol (left) and higher resolution protocol with parallel imaging (right)*

In the first patient, 7T TOF MRA correctly identified a fenestrated right MCA (middle cerebral artery) in the patient with history of ICA dissection. The full axial MIP alongside an oblique MIP showing the fenestration is given in Figure 6.3. In the second patient, MRA showed near total signal dropout of left-sided circulation beyond the first segment of the MCA, consistent with signal saturation due to slow flow through a critically

stenosed left ICA (Figure 6.4). In the third patient, MRA showed great anatomic detail in a collection of small vessels constituting a large AVM, as shown in Figure 6.5.

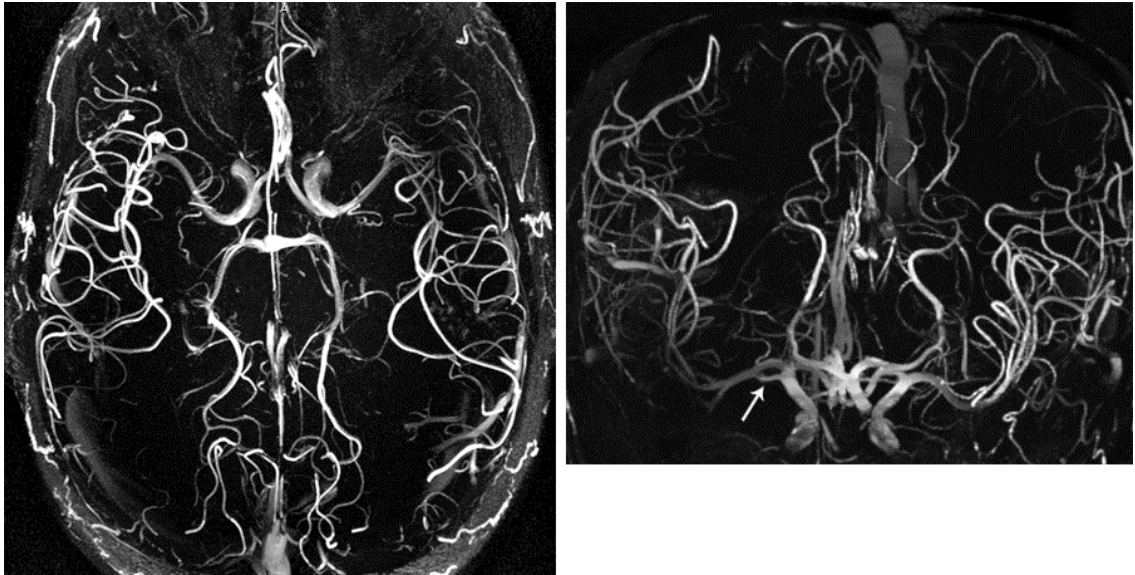


*Figure 6.3 – Full axial MIP (left) and oblique frontal MIP (right) of image data from second patient, showing fenestrated right MCA (white arrow)*





*Figure 6.4 - Full axial MIP through images acquired from patient with stenosis of left MCA*

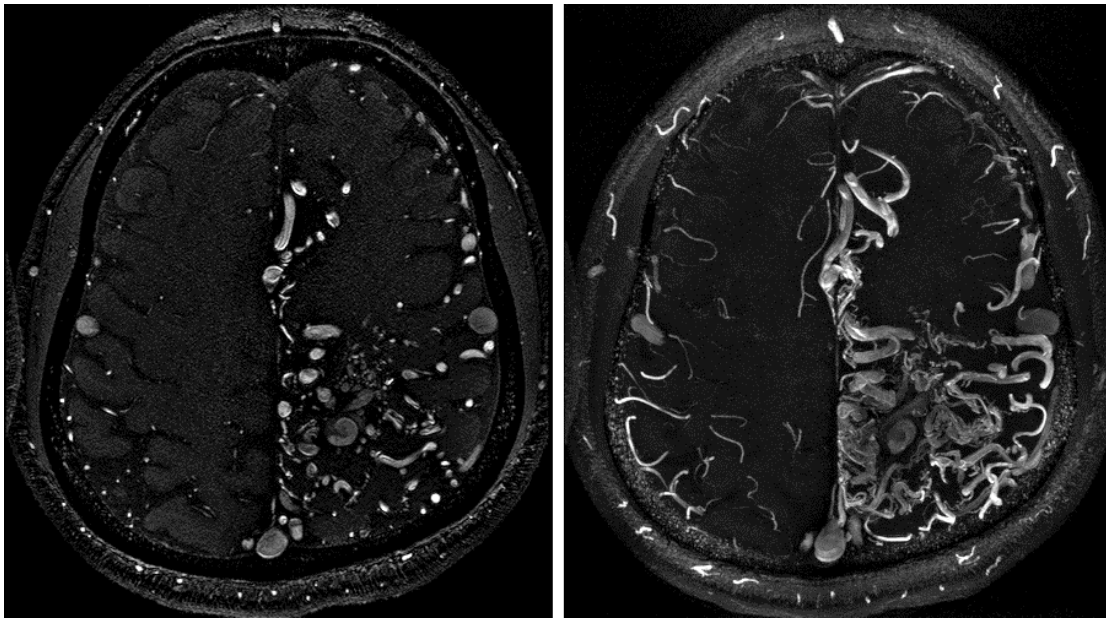


*Figure 6.5 - Axial slice (left) within AVM of patient three, alongside 10-mm axial MIP through AVM (right)*



## **6.5 Discussion**

Excellent results were obtained despite an expected 60% SNR loss associated with the new higher resolution protocol (after estimating the effects of resolution and signal averaging changes), indicating that resolution dependent effects may be reduced in some vessels.

GRAPPA-based parallel imaging techniques are better suited than SENSE [16] for maximum resolution scans, which demand a tight phase encoding FOV (e.g. 16.5cm RL as used in this study), since they are not vulnerable to reconstruction artifacts resulting from small amounts of phase wrap in the full FOV [82]. For example, the small amount of phase wrap in Fig. 4 would likely have resulted in aliasing artifact in the center of the images if reconstructed using standard SENSE, since the sensitivity calibration scan can not separate points superimposed by unintentional phase wrap.

In previous experience, the standard GRAPPA technique that was described successfully reconstructs 3T TOF MRA studies with only negligible residual aliasing artifact. Considering the unique geometry of the receiver coil used at 7T, whose non-overlapping coil layout is expected to limit the SNR losses associated with parallel imaging reconstruction [31, 34], we believe the additional terms were necessary to better model the greater coil sensitivity variation orthogonal to the phase encoding direction. Thus these coils that are intended to yield parallel imaging SNR benefits also introduce additional reconstruction challenges.

In conclusion, TOF MRA at 7T using phased array coils and a customized autocalibrating parallel imaging technique enables the non-invasive acquisition of very high resolution ( $0.146\text{mm}^3$ ) intracranial angiographic studies within a clinically feasible scan time.

## 7 Summary

In this dissertation work, I focused on the development of novel hardware and software tools to allow the improved capabilities of high field MRI with phased array coils to be realized.

In particular, I developed software tools to analyze phased array RF coils, including electromagnetic simulations to optimize coil array geometry based on SNR and parallel imaging performance calculations, and high frequency circuit modeling tools for understanding the decoupling of coil arrays using novel capacitive decoupling networks. I utilized these tools to aid in the actual hardware design and construction of a novel eight-channel receiver array for 3T MRI. I tested the performance of the coil in various applications, including MRSI, parallel DWI and musculoskeletal imaging, with excellent results in all cases.

The benefits of going to higher field strength cannot be realized without adjusting scan parameters appropriately. Standard 1.5T or even 3T scan parameters are usually far from optimal at 7T. I optimized the acquisition protocol for 7T intracranial TOF MRA, a valuable non-invasive angiographic technique, which is an excellent application for high field imaging due to the longer T1's. This technique may eventually reduce the need for more invasive alternatives, or diagnostic catheter angiography. I quantitatively demonstrated the large performance benefits of my optimized parameters over standard parameters, as well as the performance benefits of this technique in high resolution studies of 7T over 3T, the state-of-the-art in this application. To surpass CE-MRA and

compete with catheter angiography in terms of spatial resolution, I pushed the resolution even further, by developing an undersampled TOF sequence and GRAPPA-based parallel imaging reconstruction to allow the acquisition of very high resolution studies in a reasonable scan time (and reconstruction time, considering the 4.5 Gigabyte size of each MRA data set). When the standard technique (regular GRAPPA) did not perform sufficiently well in terms of residual imaging artifacts, I refined it until the performance was satisfactory. I demonstrated the effectiveness of the technique in clinical studies, in which it accurately depicted a range of cerebrovascular pathologies.

## 8 References

1. Bloch, F., W.W. Hansen, and M. Packard, *Nuclear induction*. Phys Rev, 1946. **69**(127).
2. Purcell, E.M., H.C. Torrey, and R.V. Pound, *Resonance absorption by nuclear magnetic moments in a solid*. Phys Rev, 1946. **69**(37).
3. Jin, J., *Electromagnetic Analysis and Design in Magnetic Resonance Imaging*. 1999, Boca Raton: CRC Press.
4. Haacke, E.M., et al., *Magnetic Resonance Imaging: Physical Principles and Sequence Design*. 1999, New York: John Wiley and Sons, Inc.
5. Nishimura, D.G., *Principles of Magnetic Resonance Imaging*. 1996.
6. Inan, U. and A.S. Inan, *Engineering Electromagnetics*. 1999, Menlo Park: Addison-Wesley.
7. Tropp, J., *Reciprocity and gyrotropism in magnetic resonance transduction*. Physical Review A, 2006. **74**(6): p. -.
8. Lauterbur, P., *Image Formation by Induced Local Interactions: Examples Employing Nuclear Magnetic Resonance*. Nature, 1973. **242**.
9. Macovski, A., *Noise in MRI*. Magn Reson Med, 1996. **36**(3): p. 494-7.
10. Hayes, C.E., et al., *An Efficient, Highly Homogeneous Radiofrequency Coil for Whole-Body Nmr Imaging at 1.5-T*. Journal of Magnetic Resonance, 1985. **63**(3): p. 622-628.
11. Glover, G.H., et al., *Comparison of Linear and Circular-Polarization for Magnetic-Resonance Imaging*. Journal of Magnetic Resonance, 1985. **64**(2): p. 255-270.
12. Edelstein, W.A., et al., *Surface coil magnetic resonance imaging*. Jama, 1985. **253**(6): p. 828.
13. Roemer, P.B., et al., *The NMR phased array*. Magn Reson Med, 1990. **16**(2): p. 192-225.
14. Sodickson, D.K. and C.A. McKenzie, *A generalized approach to parallel magnetic resonance imaging*. Med Phys, 2001. **28**(8): p. 1629-43.
15. Griswold, M.A., et al., *Generalized autocalibrating partially parallel acquisitions (GRAPPA)*. Magn Reson Med, 2002. **47**(6): p. 1202-10.
16. Pruessmann, K.P., et al., *SENSE: sensitivity encoding for fast MRI*. Magn Reson Med, 1999. **42**(5): p. 952-62.
17. Sodickson, D.K. and W.J. Manning, *Simultaneous acquisition of spatial harmonics (SMASH): fast imaging with radiofrequency coil arrays*. Magn Reson Med, 1997. **38**(4): p. 591-603.
18. Lupo, J.M., et al., *Feasibility of dynamic susceptibility contrast perfusion MR imaging at 3T using a standard quadrature head coil and eight-channel phased-array coil with and without SENSE reconstruction*. J Magn Reson Imaging, 2006. **24**(3): p. 520-9.
19. NCHS, <http://www.cdc.gov/nchs/fastats/deaths.htm>. 2004.
20. Ross, R., *The pathogenesis of atherosclerosis: a perspective for the 1990s*. Nature, 1993. **362**(6423): p. 801-9.

21. Willinsky, R.A., et al., *Neurologic complications of cerebral angiography: prospective analysis of 2,899 procedures and review of the literature*. Radiology, 2003. **227**(2): p. 522-8.
22. Lell, M.M., et al., *New techniques in CT angiography*. Radiographics, 2006. **26**(Suppl 1): p. S45-62.
23. McCullough, P.A., et al., *Risk prediction of contrast-induced nephropathy*. Am J Cardiol, 2006. **98**(6A): p. 27K-36K.
24. Brenner, D., et al., *Estimated risks of radiation-induced fatal cancer from pediatric CT*. AJR Am J Roentgenol, 2001. **176**(2): p. 289-96.
25. Brenner, D.J. and E.J. Hall, *Computed tomography--an increasing source of radiation exposure*. N Engl J Med, 2007. **357**(22): p. 2277-84.
26. Bernstein, M.A., K. King, and X.J. Zhou, *Handbook of MRI Pulse Sequences*. 2004: Academic Press.
27. Cowper, S.E., et al., *Scleromyxoedema-like cutaneous diseases in renal-dialysis patients*. Lancet, 2000. **356**(9234): p. 1000-1.
28. Kuo, P.H., et al., *Gadolinium-based MR contrast agents and nephrogenic systemic fibrosis*. Radiology, 2007. **242**(3): p. 647-9.
29. Penfield, J.G. and R.F. Reilly, Jr., *What nephrologists need to know about gadolinium*. Nat Clin Pract Nephrol, 2007. **3**(12): p. 654-68.
30. USRDS, *ESRD Incidence and Prevalence, in 2007 Annual Data Report*.
31. Von Morze, C., et al., *An eight-channel, nonoverlapping phased array coil with capacitive decoupling for parallel MRI at 3 T*. Concepts in Magnetic Resonance Part B-Magnetic Resonance Engineering, 2007. **31B**(1): p. 37-43.
32. Xu, D., et al., *Spectroscopic imaging of the brain with phased-array coils at 3.0 T*. Magn Reson Imaging, 2006. **24**(1): p. 69-74.
33. Jaermann, T., et al., *SENSE-DTI at 3 T*. Magn Reson Med, 2004. **51**(2): p. 230-6.
34. Weiger, M., et al., *Specific coil design for SENSE: a six-element cardiac array*. Magn Reson Med, 2001. **45**(3): p. 495-504.
35. de Zwart, J.A., et al., *Design of a SENSE-optimized high-sensitivity MRI receive coil for brain imaging*. Magn Reson Med, 2002. **47**(6): p. 1218-27.
36. Zhu, Y., et al., *Highly parallel volumetric imaging with a 32-element RF coil array*. Magn Reson Med, 2004. **52**(4): p. 869-77.
37. Pozar, D.M., *Microwave Engineering*. 1997: Wiley.
38. Tropp, J. and T. Schirmer, *Spatial dependence of a differential shading artifact in images from coil arrays with reactive cross-talk at 1.5 T*. J Magn Reson, 2001. **151**(1): p. 146-51.
39. Zhang, X. and A. Webb, *Design of a capacitively decoupled transmit/receive NMR phased array for high field microscopy at 14.1T*. J Magn Reson, 2004. **170**(1): p. 149-55.
40. Leth, H., et al., *Use of brain lactate levels to predict outcome after perinatal asphyxia*. Acta Paediatr, 1996. **85**(7): p. 859-64.
41. Bruhn, H., et al., *Proton NMR spectroscopy of cerebral metabolic alterations in infantile peroxisomal disorders*. J Comput Assist Tomogr, 1992. **16**(3): p. 335-44.
42. Felber, S.R., et al., *Maple Syrup Urine Disease - Metabolic Decompensation Monitored by Proton Magnetic-Resonance-Imaging and Spectroscopy*. Annals of Neurology, 1993. **33**(4): p. 396-401.

43. Pietz, J., et al., *Phenylketonuria: findings at MR imaging and localized in vivo H-1 MR spectroscopy of the brain in patients with early treatment*. Radiology, 1996. **201**(2): p. 413-20.
44. Vigneron, D.B., et al., *Three-dimensional proton MR spectroscopic imaging of premature and term neonates*. American Journal of Neuroradiology, 2001. **22**(7): p. 1424-1433.
45. Inder, T., et al., *Early detection of periventricular leukomalacia by diffusion-weighted magnetic resonance imaging techniques*. Journal of Pediatrics, 1999. **134**(5): p. 631-634.
46. Berman, J.I., et al., *Quantitative diffusion tensor MRI fiber tractography of sensorimotor white matter development in premature infants*. Neuroimage, 2005. **27**(4): p. 862-71.
47. Dumoulin, C.L., et al., *Magnetic resonance imaging compatible neonate incubator*. Concepts in Magnetic Resonance, 2002. **15**(2): p. 117-128.
48. Bammer, R., *Basic principles of diffusion-weighted imaging*. Eur J Radiol, 2003. **45**(3): p. 169-84.
49. Schaefer, P.W., et al., *Diffusion-weighted imaging in acute stroke*. Magn Reson Imaging Clin N Am, 2006. **14**(2): p. 141-68.
50. Sundgren, P.C., et al., *Diffusion tensor imaging of the brain: review of clinical applications*. Neuroradiology, 2004. **46**(5): p. 339-50.
51. Jaermann, T., et al., *Influence of SENSE on image properties in high-resolution single-shot echo-planar DTI*. Magn Reson Med, 2006. **55**(2): p. 335-42.
52. Dietrich, O., et al., *Influence of parallel imaging and other reconstruction techniques on the measurement of signal-to-noise ratios*. Proc Intl Soc Mag Reson Med, 2005. **13**: p. #00158.
53. Herminghaus, S., et al., *Increased choline levels coincide with enhanced proliferative activity of human neuroepithelial brain tumors*. NMR Biomed, 2002. **15**(6): p. 385-92.
54. Saks, V.A., et al., *Role of Creatine-Phosphokinase in Cellular Function and Metabolism*. Canadian Journal of Physiology and Pharmacology, 1978. **56**(5): p. 691-706.
55. Osorio, J.A., et al., *3D 1H MRSI of brain tumors at 3.0 Tesla using an eight-channel phased-array head coil*. J Magn Reson Imaging, 2007. **26**(1): p. 23-30.
56. Stubbs, M., R.L. Veech, and J.R. Griffiths, *Tumor metabolism: the lessons of magnetic resonance spectroscopy*. Adv Enzyme Regul, 1995. **35**: p. 101-15.
57. Guo, X.E. and C.H. Kim, *Mechanical consequence of trabecular bone loss and its treatment: a three-dimensional model simulation*. Bone, 2002. **30**(2): p. 404-14.
58. Majumdar, S., *Magnetic resonance imaging of trabecular bone structure*. Top Magn Reson Imaging, 2002. **13**(5): p. 323-34.
59. Wehrli, F.W., et al., *Visualization and analysis of trabecular bone architecture in the limited spatial resolution regime of in vivo micro-MRI*. Adv Exp Med Biol, 2001. **496**: p. 153-64.
60. Banerjee, S., et al., *Application of refocused steady-state free-precession methods at 1.5 and 3 T to in vivo high-resolution MRI of trabecular bone: simulations and experiments*. J Magn Reson Imaging, 2005. **21**(6): p. 818-25.

61. Banerjee, S., et al., *Autocalibrating parallel imaging of in vivo trabecular bone microarchitecture at 3 Tesla*. Magn Reson Med, 2006. **56**(5): p. 1075-84.
62. Banerjee, S., et al., *Parallel imaging of trabecular bone micro-architecture using an autocalibrating technique at 3 T*. Proc Intl Soc Mag Reson Med, 2006. **14**.
63. Dawkins, A.A., et al., *Complications of cerebral angiography: a prospective analysis of 2,924 consecutive procedures*. Neuroradiology, 2007. **49**(9): p. 753-9.
64. Drangova, M. and N.J. Pelc, *Artifacts and signal loss due to flow in the presence of B(o) inhomogeneity*. Magn Reson Med, 1996. **35**(1): p. 126-30.
65. Bernstein, M.A., et al., *High-resolution intracranial and cervical MRA at 3.0T: technical considerations and initial experience*. Magn Reson Med, 2001. **46**(5): p. 955-62.
66. Wansapura, J.P., et al., *NMR relaxation times in the human brain at 3.0 tesla*. Journal of Magnetic Resonance Imaging, 1999. **9**(4): p. 531-538.
67. Parker, D.L., C. Yuan, and D.D. Blatter, *MR angiography by multiple thin slab 3D acquisition*. Magn Reson Med, 1991. **17**(2): p. 434-51.
68. Gibbs, G.F., et al., *3.0-Tesla MR angiography of intracranial aneurysms: comparison of time-of-flight and contrast-enhanced techniques*. J Magn Reson Imaging, 2005. **21**(2): p. 97-102.
69. Gibbs, G.F., et al., *Improved image quality of intracranial aneurysms: 3.0-T versus 1.5-T time-of-flight MR angiography*. AJNR Am J Neuroradiol, 2004. **25**(1): p. 84-7.
70. Suarez, J.I., R.W. Tarr, and W.R. Selman, *Aneurysmal subarachnoid hemorrhage*. N Engl J Med, 2006. **354**(4): p. 387-96.
71. Hop, J.W., et al., *Case-fatality rates and functional outcome after subarachnoid hemorrhage: a systematic review*. Stroke, 1997. **28**(3): p. 660-4.
72. Al-Kwif, O., D.J. Emery, and A.H. Wilman, *Vessel contrast at three Tesla in time-of-flight magnetic resonance angiography of the intracranial and carotid arteries*. Magn Reson Imaging, 2002. **20**(2): p. 181-7.
73. Eissa, A. and A. Wilman, *3D TOF MRA of the intracranial arteries: effects of increasing magnetic field to 4.7T*. Proc Intl Soc Mag Reson Med, 2006. **14**: p. #1945.
74. Heverhagen, J., et al., *Ultrahigh field (>7T) time-of-flight and phase contrast magnetic resonance angiography of the intracerebral arteries*. Proc Intl Soc Mag Reson Med, 2006. **14**: p. #814.
75. Wiggins, G.C., et al., *Eight-channel phased array coil and detunable TEM volume coil for 7 T brain imaging*. Magn Reson Med, 2005. **54**(1): p. 235-40.
76. von Morze, C., et al., *Intracranial time-of-flight MR angiography at 7T with comparison to 3T*. J Magn Reson Imaging, 2007. **26**(4): p. 900-4.
77. Ledden, P., P. van Gelderen, and J. Duyn, *Birdcage Volume Transmit, Eight Channel Receive Array System for Brain Imaging at 7T*. Proc Intl Soc Mag Reson Med, 2005. **13**: p. #322.
78. Haacke, E., et al., *Magnetic Resonance Imaging: Physical Principles and Sequence Design*. 1999: p. 713,876.
79. Edelstein, W.A., et al., *The intrinsic signal-to-noise ratio in NMR imaging*. Magn Reson Med, 1986. **3**(4): p. 604-18.



80. Wang, Z., J. Wang, and J.A. Detre, *Improved data reconstruction method for GRAPPA*. Magn Reson Med, 2005. **54**(3): p. 738-42.
81. Wald, L.L., et al., *Phased array detectors and an automated intensity-correction algorithm for high-resolution MR imaging of the human brain*. Magn Reson Med, 1995. **34**(3): p. 433-9.
82. Griswold, M.A., et al., *Field-of-view limitations in parallel imaging*. Magn Reson Med, 2004. **52**(5): p. 1118-26.

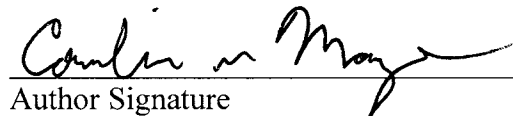
UCSF Library Release

**Publishing Agreement**

*It is the policy of the University to encourage the distribution of all theses and dissertations. Copies of all UCSF theses and dissertations will be routed to the library via the Graduate Division. The library will make all theses and dissertations accessible to the public and will preserve these to the best of their abilities, in perpetuity.*

***Please sign the following statement:***

*I hereby grant permission to the Graduate Division of the University of California, San Francisco to release copies of my thesis or dissertation to the Campus Library to provide access and preservation, in whole or in part, in perpetuity.*

  
\_\_\_\_\_  
Author Signature

1/17/2008  
Date